METHODS FOR MITIGATING THE EFFECT OF NOISE, INTERFERENCE, AND MODEL ERROR ON MICROWAVE BREAST IMAGING

by

Matthew J. Burfeindt

A dissertation submitted in partial fulfillment of
the requirements for the degree of

Doctor of Philosophy

(Electrical Engineering)

at the

UNIVERSITY OF WISCONSIN–MADISON

2013

Date of final oral examination: 5/14/2013

The dissertation is approved by the following members of the Final Oral Committee:

Susan C. Hagness, Professor, Electrical and Computer Engineering
Barry D. Van Veen, Professor, Electrical and Computer Engineering
Nader Behdad, Assistant Professor, Electrical and Computer Engineering
Walter F. Block, Professor, Biomedical Engineering
Frederick Kelcz, Associate Professor, Radiology

ACKNOWLEDGMENTS

I would first like to thank my advisors, Profs. Susan Hagness and Barry Van Veen, for the wise counsel and education they have provided me over the past five years. I'd also like to thank Prof. Nader Behdad for research-related guidance; Prof. Ezekiel Bahar, for helping to put me on my current path; and my SMART program mentors, Robert Orgusaar and Dr. Jason Foley, for advice and professional development.

Thanks to current and past graduate students Dr. Jacob Shea, Dr. Suzette Aguilar, Dr. Earl Zastrow, Dr. Steve Kennedy, Dr. Keely Willis, Dr. Min Zhao, Dr. Al Mashal, TJ Colgan, Owen Mays, Fuqiang Gao, Adam Weiss, and many others for countless hours of assistance and companionship.

Lastly, I'd like to thank those closest to me. Thanks to my parents, Joel and Janel, for encouraging my pursuits and for providing me with a lifetime of warmth and affection. Thanks to Amanda and Jason, for their friendship. And thanks to Rachel, for endless support and optimism.

My research was supported by the Department of Defense SMART Scholarship for Service program, the National Institutes of Health, and Fairview Microwave.

ABSTRACT

Microwave inverse scattering shows promise for meeting important clinical needs in breast imaging that arise due to drawbacks in traditional imaging technologies. The dielectric contrast between different breast tissue types, the 3-D nature of various inverse scattering algorithms, as well as microwave technology's relative safety and low cost motivate a microwave-based approach. However, challenges remain for this type of imaging technique, as it requires solving a linear system that is ill-posed and underdetermined, thus making it sensitive to noise, interference, and mismatch between the assumed and actual properties of the propagation environment. In this document, we report a series of studies performed with the goal of mitigating the effect of these types of signal errors on the imaging results. We conduct a numerical feasibility study to demonstrate the efficacy of microwave breast imaging using an enclosed array of miniaturized, multi-band patch antennas designed to account for the ill-posed nature of the imaging problem. We then conduct several experimental studies with an array prototype, wherein we characterize the sensitivity of the array to model error as well as create experimental reconstructions of both geometrically-simple objects and an MRI-derived 3-D-printed breast phantom. Lastly, we incorporate a beamforming-enhancement into the imaging algorithm with the goal of making it less sensitive to signal error.

TABLE OF CONTENTS

Page

LIST OF TABLES

LIST OF FIGURES

Figure Page

Figure Page

Chapter 1

Introduction

Breast cancer is a very frequently diagnosed disease and a common cause of death for women. It has the highest incidence rate among cancers for women in the United States. The incidence rate for the next most frequently diagnosed cancer (lung cancer) is less than one half the incidence rate for breast cancer. The average woman has an estimated 12.2% lifetime risk of developing the disease and a 2.8% lifetime risk of dying from it [2]. Breast cancer is therefore a significant public health concern and motivates development of improved techniques for both screening and prevention.

Early detection allows for earlier intervention and thus more positive outcomes. X-ray mammography is the dominant technique for breast cancer screening. Numerous studies have shown it to decrease the mortality rate from breast cancer [3–5]. Despite its benefits, X-ray mammography has several well-known drawbacks. It uses ionizing radiation and uncomfortable breast compression, which might deter some patients from regular screening. It creates two-dimensional (2-D) projections of breast density, as opposed to approximations of the three-dimensional (3-D) tissue structure. The mammographic appearance of tumors is sometimes similar to the appearance of benign lesions [6]. Thus, X-ray mammography suffers from a high rate of false positives (i.e., it has low specificity). A study by Elmore et al. [7] showed that 24% of women experienced a false positive over a ten-year span of regular mammography screenings. False positives have both physical costs, due to the need for follow-up examinations that may include invasive biopsies, and psychological costs [8]. Mammography also has a significant false-negative rate ranging from 10% to

25% [9] (i.e., it has low sensitivity). High breast density is considered a major complicating factor leading to false negatives [10].

Several other modalities are sometimes used as complements to X-ray mammography. Magnetic Resonance Imaging (MRI) can create highly detailed tomographic breast images, and thus can detect some tumors that are missed by mammography. However, MRI has a higher false positive rate. MRI is also relatively time-consuming and expensive. Ultrasound sonography is often used as a follow-up procedure after a mammogram has detected a possible tumor. It can sometimes differentiate between tumors and benign lesions. However, sonography operates in real time, is very user-dependent, and also has a high false positive rate. Neither MRI nor sonography are recommended as stand-alone techniques for breast cancer screening [11].

While imaging techniques have long played a role in screening and diagnosis of breast cancer, breast imaging ultimately may also play a larger role in individualized risk assessment and therefore preventative intervention. Quantitative breast density evaluation in particular shows promise due to the correlation between breast density and breast cancer risk. Numerous studies have suggested that high breast density increases the risk for breast cancer between four and six times [12, 13]. Furthermore, an increase in breast density over time is associated with an increase with breast cancer risk, whereas a decrease in breast density is associated with a decrease in risk [14, 15]. Routine breast density evaluation and tracking could thus serve as the basis for decisions on influencing breast density via hormonal treatment for at-risk patients.

Breast density is typically evaluated via the X-ray mammogram, either through visual inspection or with the aid of computer-assisted planimetry. Quantitative evaluation of breast density involves estimating the percentage of the breast consisting of epithelial or connective tissue, collectively referred to as *fibroglandular tissue*, as opposed to *adipose* tissue. Ambiguity in density evaluation with the mammogram arises due to the inherent limitations in estimating a 3-D volumetric density from a 2-D projection. Routine use of conventional 3-D modalities, such as MRI, for density evaluation are constrained due to cost.

Microwave imaging via inverse scattering has the potential to address the clinical needs in breast imaging that arise due to the weaknesses in X-ray mammography and other traditional

imaging techniques. This modality involves using an array of microwave antennas to transmit low-power electric fields into the breast volume. The array records the fields transmitted through and reflected from the breast and processes them via an inverse scattering algorithm in order to create a 3-D quantitative estimation of the breast's distribution of dielectric properties. The dielectric contrast between adipose tissue, fibroglandular tissue, and malignant tissue serves as the basis for a microwave-based approach. Microwave images of the 3-D tissue structure could be used for monitoring breast density, screening and diagnosis of breast cancer (perhaps using contrast agents), or monitoring of breast cancer treatment. Microwave breast imaging would operate comfortably (without breast compression) and at low power while using a non-ionizing portion of the electromagnetic spectrum.

A major challenge in microwave imaging via inverse scattering is that it involves solving a system of linear equations that is ill-posed and underdetermined. Small perturbations in the recorded signal can cause the imaging algorithm to either diverge or converge to an incorrect solution. The fidelity of a dielectric reconstruction is strongly influenced by the electric field spatial sampling density, the number of discrete frequencies used for a solution, and the extent to which noise, interference, or model error is allowed to corrupt the scattered field vector [16, 17]. There is thus interest in developing antenna arrays that are designed taking the above considerations into account, as well as in improving existing imaging algorithms in order to make them more robust to scattered field corruption.

Aguilar et al. [18] have previously introduced an enclosed array of miniaturized, multi-band patch antennas. The array is shielded on all sides by conducting ground planes in order to isolate the imaging region from outside interference. The array elements are designed in order to radiate efficiently at multiple bands of interest while maintaining a small footprint, thus allowing for a dense antenna population. The array has the additional benefit in that it fits into the interstitial space of an MRI patient support platform, allowing for a microwave data acquisition to proceed directly after an MR scan so that the resulting microwave image can be co-registered and compared unambiguously to the MR benchmark image. The favorable features of the array motivate preclinical imaging studies in order to more robustly validate feasibility.

Further mitigation of the ill-posed nature of the inverse problem may be achieved through the addition of focusing techniques into the imaging algorithm. Focusing on transmit and receive lessens the influence of noise on the dielectric reconstruction, as signal is added coherently, while noise is not, which leads to an increase in the effective signal-to-noise ratio (SNR) of the system. Incorporating beamforming techniques [19] into the imaging algorithm allows this focusing to be accomplished based on the assumed propagation environment of the imaging domain.

This document reports the results of a series of studies conducted with the goal of developing approaches that mitigate the effects of the ill-posed nature of microwave breast imaging via inverse scattering. These studies encompass pre-clinical imaging studies using an array of miniaturized, multi-band patch antennas, as well as the incorporation and evaluation of transmit-receive beamforming techniques into the microwave imaging algorithm. To this end, the studies fulfill five specific aims:

1. **Microwave imaging of numerical breast phantoms using an enclosed array of miniaturized, multi-band patch antennas.** Dielectric reconstructions of MRI-derived numerical phantoms are created based on a simulated data acquisition. The reconstructions compare favorably with previous reconstructions using idealized arrays. This study demonstrates the theoretical feasibility of using such an array for microwave breast imaging.

2. **Characterization of model error for an experimental array prototype.** The mismatch between the assumed and actual properties of the propagation environment of the array, or its model error, is characterized by comparing simulated and measured signals for the empty array. A sensitivity study is then performed, wherein various features of the array are perturbed in simulation in order to determine which sorts of array imperfections are most likely to lead to significant signal corruption.

3. **Preliminary experimental imaging of simple objects using an array of miniaturized multi-band patch antennas.** Reconstructions of glycerol solution tubes and a 3-D-printed

square cylindrical phantom are reported. The results demonstrate the ability of the experimental imaging hardware and algorithm to accurately reconstruct target distributions of varying size and configuration.

4. **Development and experimental imaging of an MRI-derived 3-D-printed breast phantom.** Such a phantom provides an imaging test object with a more complicated and anatomically relevant geometry. The method for construction of the phantom is discussed. Promising experimental imaging results are then reported. These results demonstrate the ability of the imaging system to reconstruct dielectric profiles derived from realistic and complex tissue distributions.

5. **Numerical investigation of beamforming-enhanced microwave breast imaging.** The incorporation of transmit-receive beamforming into the inverse scattering algorithm is described. Numerical breast phantoms are imaged from simulated data acquisition for varying SNR using both the beamforming-enhanced and standard inverse scattering algorithms. The beamforming-enhanced algorithm is shown to be less sensitive to scattered signal corruption.

The remainder of this document is organized as follows. Chapter 2 describes the background and significance of microwave breast imaging, including its theoretical formulation as well as past work. Chapters 3 through 7 report the results of studies performed in support of Aims 1 through 5, respectively. Lastly, Chapter 8 proposes future work.

Chapter 2

Background and Significance of Microwave Breast Imaging

Non-invasive medical imaging has progressed greatly in the past century. However, the most widely-used imaging techniques, such as magnetic resonance imaging (MRI), ultrasound sonography, computed tomography (CT), proton emission tomography (PET), and X-ray mammography each have well-documented limitations. These limitations include high cost (in the cases of MRI, CT and PET) and lack of specificity (in the cases of X-ray mammography, MRI, and ultrasound sonography for breast imaging). There is thus a clinical need for competing low-cost medical imaging technologies.

There has been interest in microwave-based approaches as possible complements or replacements to current techniques in recent years. Microwaves are attractive for medical imaging because of the variance in water content between different types of tissues, which allows for microwave scattering and thus differentiation between anatomical structures. Microwave wavelengths are relevant for the medical imaging regime. Electromagnetic waves are non-ionizing in the microwave regime, and thus relatively safe at low power. Lastly, microwave technology is widely available and low-cost, as compared to imaging techniques such as MRI.

While microwave imaging is thus very promising, it also poses several important challenges. Microwaves propagating in the human body undergo multiple (and thus non-linear) scattering. Biological tissue is often lossy, so penetration is limited for small wavelengths. Reflection from the skin is substantial and must be considered in the imaging process.

Microwave imaging has been explored for a number of different medical applications, such as brain imaging for stroke management [20,21], cardiac imaging for monitoring infarctions [22,23],

bone imaging for mineralization evaluation [24], and imaging of the lungs [25] and breast for cancer screening. Microwave breast imaging in particular has received a great deal of attention due to several properties of the breast that are convenient for microwave imaging. The breast lies outside the body cavity, which facilitates microwave penetration. The breast is relatively electrically small at microwave frequencies, which makes it easier to numerically simulate for the purpose of algorithmic development. A major component of the breast is adipose tissue, which is low-loss at microwave frequencies. The dielectric contrast between adipose tissue and the structural components of the breast, which are made up of fibroglandular tissue, is significant. Studies have also shown a dielectric contrast between healthy and malignant breast tissue. These contrasts in dielectric properties allow for discrimination between different tissue structures on a microwave image, and thus form the physical basis for imaging the breast in the microwave regime.

2.1 Dielectric properties of breast tissue

The electric field scattered by the breast volume is a function of its spatial distribution of dielectric properties (i.e., its dielectric profile.) Microwave imaging algorithms attempt to create a mapping of the dielectric profile in the imaging region (either quantitatively or qualitatively) by acting on the scattered field. The dielectric properties of the breast are relevant to breast imaging because the dielectric properties of biological tissue are highly correlated with water content, and thus tissue density.

The dielectric properties of a material are commonly described by its complex electric permittivity, ε^*. Assuming an $e^{j\omega t}$ time dependence in the electric field, the electric permittivity at frequency ω can be written as $\varepsilon^*(\omega) = \varepsilon_0\varepsilon_r(\omega) - j\sigma_{\text{eff}}(\omega)/\omega$, where ε_0 is the permittivity of free space, ε_r is the relative permittivity (sometimes referred to as the dielectric constant, or simply the permittivity) which is related to the ability of the material to be electrically polarized, σ_{eff} is the effective conductivity, which determines the electric field propagation loss of the material, and $j = \sqrt{-1}$.

Numerous studies have reported a large measured contrast between the dielectric properties of cancerous breast tissue and the dielectric properties of normal tissue [26–31]. This measured large

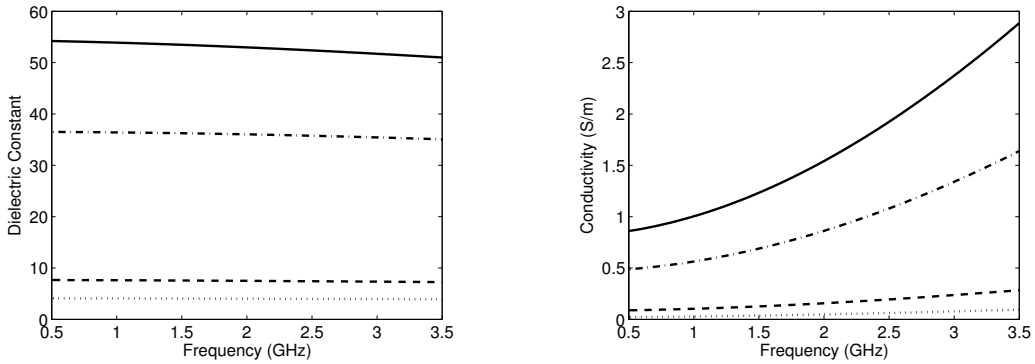

(a) **(b)**

Figure 2.1: (a) Dielectric constant and (b) conductivity for breast tissue types, from the Cole-Cole models given in [1]. Solid line: 75th percentile fibroglandular tissue. Dash-dot line: 25th percentile fibroglandular tissue. Dash-dash line: 75th percentile adipose tissue. Dot-dot line: 25th percentile adipose tissue.

contrast, which ranged roughly from 2:1 to 10:1, was an encouraging indicator for the feasibility for microwave imaging for breast cancer. Unfortunately, the studies published prior to 2007 suffered from numerous deficiencies. Only one study measured dielectric properties above 3.2 GHz. The studies didn't measure many different types of tissues found in the breast, and were conducted using a limited number of subjects.

The large-scale study by Lazebnik et al. published in 2007 [32] measured the dielectric properties of breast tissue from over 100 subjects obtained following breast cancer surgery. Measurements were conducted from 0.5 to 20 GHz for adipose, fibroglandular, benign, and malignant tissue. Dielectric constant and conductivity for various breast tissue types, as given by Cole-Cole dispersion curves from [1] fitted to the data from [32], are shown in Fig. 2.1. The study showed that the dielectric properties of breast tissue varied greatly according to the amount of adipose tissue in the sample. The dielectric properties of high-adipose tissue (fatty tissues) showed an order-of-magnitude difference from the dielectric properties of low-adipose tissues (fibroglandular tissues). In addition, the study reported a mean contrast of 10:1 between malignant and healthy

adipose tissue and a mean contrast of 1.1:1 between malignant and healthy fibroglandular tissue. This latter contrast is important since most tumors originate in fibroglandular tissue.

Breast tissue at microwave frequencies is dispersive. The frequency dependence of the dielectric parameters must be taken into account when implementing a microwave imaging algorithm for the breast. The dispersive complex permittivity of a material can be modeled as a function of frequency ω by a multi-pole Debye model:

$$\varepsilon^*/\varepsilon_0 = \varepsilon_\infty + (\varepsilon_s - \varepsilon_\infty) \sum_{n=1}^{N} \frac{1}{1 + j\omega\tau_n} + \frac{\sigma_s}{j\omega\varepsilon_0} \tag{2.1}$$

The infinite permittivity ε_∞ is the high frequency limit of the dielectric constant, whereas ε_s is the low-frequency limit. The number of Debye poles is N, the relaxation time for the nth pole is τ_n, and the static conductivity σ_s is the low-frequency limit of conductivity. The expression $\varepsilon_s - \varepsilon_\infty$ can be combined into a single term, $\Delta\varepsilon$, the delta permittivity. It is common for multi-pole Debye models to use a separate delta permittivity term for each Debye pole; however, in this document we will use models with the same $\Delta\varepsilon$ for all poles. In Chapters 3 and 7, the dispersive dielectric profiles of the objects under test will be estimated by reconstructing the Debye parameters ε_∞, $\Delta\varepsilon$, and σ_s at each voxel in the imaging domain, while in Chapters 5 and 6, only ε_∞ and $\Delta\varepsilon$ are reconstructed.

2.2 Prior work in microwave breast imaging

Two main types of active microwave techniques have been explored for the breast imaging application: radar-based techniques and inverse-scattering techniques. Radar-based techniques approximate the locations of strong scatterers in the breast. These algorithms assume that the propagation environment is linear and that tumors are strong scatterers at microwave frequencies. The goal of radar-based microwave imaging of the breast is not to quantitatively reconstruct the dielectric profile of the breast, but is instead to create a qualitative mapping of strong scatterers.

Several different types of radar-based algorithms have been explored for the breast. Confocal microwave imaging (CMI) uses a delay-and-sum (DAS) technique to compensate for propagation time from various foci in the imaging region and locate strong scatterers [33–41]. Time-reversal

techniques use back-propagation of received signals to locate scatterers [42]. Beamforming techniques improve upon CMI by taking into account dispersion and suppressing clutter [43–49].

Radar-based approaches generated enthusiasm due to their ability to locate tumors in breast phantoms. Early studies, however, mostly used phantoms with interiors that were either homogeneous (with the exception of the tumor) or varied in their dielectric properties by less than 20%. The tumors in these studies also typically had higher contrasts with their surrounding tissue (often 5:1 or greater) than would be expected based on the wide-scale study by Lazebnik et al. [32]. Bond et al. [43] tested their space-time beamforming technique on numerical breast phantoms for a variety of malignant-to-healthy dielectric contrasts and found that they were unable to discern tumor response from clutter response for the low-contrast case of 1.1:1. Klemm et al. [49] applied their radar-based algorithm to experimental phantoms of varying complexity and concluded from the results that the most significant limiting factor for radar-based breast imaging was the degree of heterogeneity of the breast.

Inverse scattering approaches to microwave breast imaging differ from radar approaches in that they use full-wave equations governing electromagnetic scattering in the breast in order to build a quantitative estimate of the dielectric profile. These approaches are usually iterative and account for nonlinear propagation that arises from the heterogeneity of fibroglandular tissue in the breast. Unlike radar-based techniques, inverse scattering techniques attempt to image not only a possible tumor, but also the surrounding structural tissue, and thus may be used for breast density evaluation and treatment monitoring in addition to cancer screening. These benefits come at the expense of a higher computational cost.

A research group at Dartmouth University led by Dr. Paul Meaney has led the field in clinical microwave inverse scattering for the breast. They were the first to publish quantitative image results from human subjects using an inverse scattering technique [50, 51]. They used a circular array of monopole antennas immersed in a saline bath for data acquisition. Each subject laid prone with her breast hanging pendant into the saline bath. The monopole array was translated to a number of different elevation planes in the tank, where data was acquired at seven frequencies up to 3 GHz. The data were used to create single-frequency tomographic reconstructions of the dielectric profile

in each elevation plane. The results were auspicious, as the outline of the breast was apparent in the slices, although little interior detail could be seen. The average dielectric properties in the reconstructions correlated well with the radiological breast density categorizations for the subjects' breasts. Meaney et al. have since made a number of improvements to their technique, including the incorporation of multiple frequency data [16] and expansion to 3-D [52].

Various studies have created dielectric reconstructions of numerical domains based on simulated data acquisitions. Such studies are useful for algorithm development and feasibility evaluation, as they allow the reconstructed domains to be compared directly to the known exact dielectric profile. Most used simple breast phantoms with unrealistic interiors and inclusions [16, 53–56]. Beginning in 2008, researchers began using MRI-derived numerical breast phantoms (e.g., [1]) which acted as more realistic test domains for numerical experiments. Such phantoms are created by mapping pixel intensity from MR images of human subjects to permittivity and conductivity in a 3-D numerical breast model. They are therefore anatomically realistic in their distributions of adipose and fibroglandular tissue.

MRI-derived numerical breast phantoms have been imaged using several different inverse scattering algorithms. Shea et al. [57] used the distorted Born iterative method (DBIM) [58] to create 3-D multi-frequency dielectric reconstructions of breast phantoms from four different density classes. The reconstructions accurately showed the shape and location of the fibroglandular tissue structures for all four classes. They later published a study [59] in which they added artificial tumors into the same four phantoms and then performed a simulated data acquisition both with and without assumed contrast enhancements from exogeneous injection of carbon nanotubes and air microbubbles [60, 61]. Differential imaging led to the tumors being accurately identified and located in the resulting microwave image.

Reconstructions of 2-D profiles formed from cross-sections of 3-D MRI-derived phantoms have been performed with accurate results using the contrast-source inversion (CSI) method [21] and the Forward-Backward Time-Stepping (FTBS) method [62]. FTBS has also been used to create 3-D reconstructions of breast phantoms with 5-10 mm tumors [63]. The FBTS method was able to locate tumors of size 10 mm well, but had more difficulty finding smaller tumors and converged to

an inaccurate solution when the dielectric contrast between the tumor and the surrounding tissue was reduced to 1.5:1.

The simulated work described above resulted in reconstructions that were of largely high quality; however, it used dense arrays of highly idealized antennas, such as small dipoles or line sources. Obtaining similar experimental performance will require an array of physically realizable antennas that have a small footprint, multiple frequencies of operation, and efficiency in radiation. These requirements are necessary in order to counteract the ill-posed nature of the system equations that is created by the imaging algorithm. The construction of this linear system, as well as other details on the inverse scattering algorithm, are described in the following section.

2.3 The Inverse scattering algorithm

For the general inverse scattering problem, L antennas are located around a volume V to be imaged. Both V and the array are located within a volume of interest D. The complex permittivity profile for all points $\mathbf{r}$ in D is given by $\varepsilon^*(\mathbf{r}) = \varepsilon_b^*(\mathbf{r}) + o(\mathbf{r})\varepsilon_0$, where $\varepsilon_b^*(\mathbf{r})$ is a known background complex permittivity profile that can be either homogeneous or heterogeneous, and $o(\mathbf{r})$ is the complex permittivity contrast. Outside V, $o(\mathbf{r}) = 0$. Inside V, $o(\mathbf{r})$ is unknown; the goal of the inverse scattering problem is to create an estimate of the unknown dielectric contrast $o(\mathbf{r})$ for all points $\mathbf{r}$ in V.

Each antenna in the array sequentially transmits an electric field pulse into V. For a given transmit antenna, let $\mathbf{E}^i(\mathbf{r})$ be the incident electric field, defined as the electric field in D assuming $\varepsilon^*(\mathbf{r}) = \varepsilon_b^*(\mathbf{r})$ for all $\mathbf{r}$. Let $\mathbf{E}^t(\mathbf{r})$ be the total electric field, defined as the electric field in D assuming $\varepsilon^*(\mathbf{r}) = \varepsilon_b^*(\mathbf{r}) + o(\mathbf{r})\varepsilon_0$. The incident field $\mathbf{E}^i(\mathbf{r})$ is known (i.e., can be computed) for all $\mathbf{r}$, while the total field $\mathbf{E}^t(\mathbf{r})$ is unknown in V and is measured at all antenna locations in the array. Let $\mathbf{E}^s(\mathbf{r})$ be the scattered field, given by $\mathbf{E}^s(\mathbf{r}) = \mathbf{E}^t(\mathbf{r}) - \mathbf{E}^i(\mathbf{r})$. Using the volume equivalence theorem and the integral form of the Helmholtz equation, the scattered field at antenna location $\mathbf{r}_{\mathrm{rec}}$ resulting from transmission of an electric field pulse from antenna location $\mathbf{r}_{\mathrm{src}}$ can be written

$$\mathbf{E}^s(\mathbf{r}_{\mathrm{src}}, \mathbf{r}_{\mathrm{rec}}) = \mathbf{E}^t(\mathbf{r}_{\mathrm{src}}, \mathbf{r}_{\mathrm{rec}}) - \mathbf{E}^i(\mathbf{r}_{\mathrm{src}}, \mathbf{r}_{\mathrm{rec}}) = \omega^2 \mu_0 \varepsilon_0 \int_V \bar{\mathbf{G}}^b(\mathbf{r}', \mathbf{r}_{\mathrm{rec}}) \mathbf{E}^t(\mathbf{r}_{\mathrm{src}}, \mathbf{r}') o(\mathbf{r}') d^3\mathbf{r}' \quad (2.2)$$

where $\bar{\mathbf{G}}^b(\mathbf{r}', \mathbf{r}_{\rm rec})$ is the background dyadic Green's function relating the field at $\mathbf{r}_{\rm rec}$ due to a unit current density at $\mathbf{r}'$, $\mathbf{E}^t(\mathbf{r}_{\rm src}, \mathbf{r}')$ is the total field at $\mathbf{r}'$ resulting from transmission of the electric field pulse at $\mathbf{r}_{\rm src}$, $\mathbf{E}^t(\mathbf{r}_{\rm src}, \mathbf{r}_{\rm rec})$ is the measured total field at source location $\mathbf{r}_{\rm rec}$ due to transmission of an electric field pulse from $\mathbf{r}_{\rm src}$, $\mathbf{E}^i(\mathbf{r}_{\rm src}, \mathbf{r}_{\rm rec})$ is the corresponding incident field obtained via numerical simulation of the background permittivity, and μ_0 is the magnetic permeability of free space. For single polarization antennas, $\mathbf{E}^s(\mathbf{r}_{\rm src}, \mathbf{r}_{\rm rec})$ reduces to a scalar, $E^s(\mathbf{r}_{\rm src}, \mathbf{r}_{\rm rec})$.

Collection of scattered fields from numerous transmit-receive channels results in a system of integral equations of the form of (2.2), which are non-linear in the unknown contrast, as the total field in the integrand is a function of $o(\mathbf{r}')$. Inverse scattering generally involves using a non-linear optimization technique to find an estimate to $o(\mathbf{r}')$ which minimizes E^s over the set of antenna transmit-receive pairs. Numerous optimization algorithms exist for solving this problem. The remainder of this section describes the distorted Born iterative method (DBIM), which is equivalent to the Gauss-Newton (GN) method [64]. Other inverse scattering algorithms include the Born iterative method (BIM) and contrast source inversion (CSI).

DBIM involves first linearizing (2.2) by replacing $\mathbf{E}^t$ with $\mathbf{E}^i$ in the integrand, a step which is known as the Born approximation, and which is valid for small contrasts. The imaging region V is then discretized into K voxels. A system of linear equations in the form $\mathbf{b} = \mathbf{A}\mathbf{x}$ is created, where $\mathbf{x}$ is the vector of unknown dielectric contrast at each voxel. For a single-pole Debye parameter reconstruction, $\mathbf{x}$ is of size $3K \times 1$ and is given by

$$\mathbf{x} = [o_{\varepsilon\infty}(\mathbf{r}'_1) \dots o_{\varepsilon\infty}(\mathbf{r}'_K) \;\; o_{\Delta\varepsilon}(\mathbf{r}'_1) \dots o_{\Delta\varepsilon}(\mathbf{r}'_K) \;\; o_{\sigma}(\mathbf{r}'_1) \dots o_{\sigma}(\mathbf{r}'_K)]^{\rm T} \tag{2.3}$$

where $\mathbf{r}'_1 \dots \mathbf{r}'_K$ are the locations of each imaging region voxel, $o_{\varepsilon\infty}$ is the contrast in ε_∞, $o_{\Delta\varepsilon}$ is the contrast in $\Delta\varepsilon$, and o_σ is the contrast in σ_s at each voxel. The $2M \times 1$ vector $\mathbf{b}$ is the vector of scattered electric fields for each antenna transmit-receive pairs, where M is the total number of

pairs. It is given by

$$\mathbf{b} = \begin{bmatrix} \Re\left\{E^s(\mathbf{r}_{\mathrm{rec}(1)}, \mathbf{r}_{\mathrm{src}(1)})\right\} \\ \vdots \\ \Re\left\{E^s(\mathbf{r}_{\mathrm{rec}(M)}, \mathbf{r}_{\mathrm{src}(M)})\right\} \\ \Im\left\{E^s(\mathbf{r}_{\mathrm{rec}(1)}, \mathbf{r}_{\mathrm{src}(1)})\right\} \\ \vdots \\ \Im\left\{E^s(\mathbf{r}_{\mathrm{rec}(M)}, \mathbf{r}_{\mathrm{src}(M)})\right\} \end{bmatrix} \tag{2.4}$$

where $\Re$ and $\Im$ are the real and imaginary parts, respectively. Let the submatrix $\mathbf{A}^0$ be of size $M \times K$, where the mth row of $\mathbf{A}^0$ is formed by discretizing the kernel of the integral equation (2.2) for the mth transmit-receive pair. The $m-k$ component of $\mathbf{A}^0$ is then given by

$$A^0_{mk} = \Delta^3 \omega^2 \mu_0 \varepsilon_0 \bar{\mathbf{G}}^{\mathbf{b}}(\mathbf{r}'_k, \mathbf{r}_{\mathrm{rec}(m)}) \mathbf{E}^i(\mathbf{r}_{\mathrm{src}(m)}, \mathbf{r}'_k) \hat{\mathbf{p}} \tag{2.5}$$

In (2.5), Δ^3 is the volume of one voxel in the imaging region and $\hat{\mathbf{p}}$ is the unit vector representing the polarization direction of the antennas. The matrix $\mathbf{A}$ is then given by

$$\mathbf{A} = \begin{bmatrix} \Re\{\mathbf{A}^0\} & \Re\{c_\Delta\}\Re\{\mathbf{A}^0\} - \Im\{c_\Delta\}\Im\{\mathbf{A}^0\} & -\Im\{c_\sigma\}\Im\{\mathbf{A}^0\} \\ \Im\{\mathbf{A}^0\} & \Im\{c_\Delta\}\Re\{\mathbf{A}^0\} + \Re\{c_\Delta\}\Im\{\mathbf{A}^0\} & +\Im\{c_\sigma\}\Re\{\mathbf{A}^0\} \end{bmatrix}, \tag{2.6}$$

where $c_\Delta = (1 + j\omega\tau)^{-1}$ and $c_\sigma = (j\omega\varepsilon_0)^{-1}$. The size of $\mathbf{A}$ is $2M \times 3K$. It is equivalent to the Jacobian matrix used by GN. Multiple frequency reconstructions may be performed by creating $\mathbf{b}$ and $\mathbf{A}$ for each frequency and then vertically concatenating.

Since the background dielectric profile is known, the Green's function and incident field quantities in (2.5) may be found via full-wave electromagnetic simulation of the background profile using a technique such as the finite-difference time-domain (FDTD) or finite-element (FEM) methods. Such simulation techniques solve the Helmholtz equation

$$\nabla^2 \mathbf{E}^i + \omega^2 \mu_0 \varepsilon_b^* \mathbf{E}^i = j\omega\mu_0 \mathbf{J} \tag{2.7}$$

for the incident field due to the source current density, $\mathbf{J}$. This simulation step is commonly referred to as the *forward solution*, and is often computationally expensive. The incident field is typically computed at each voxel in the imaging domain for every transmit antenna. The Green's function

for every voxel and receive antenna combination can then be computed from the incident field and source conditions using the integral form of the Helmholtz equation,

$$\mathbf{E}^i(\mathbf{r}_{\mathrm{src}}, \mathbf{r}') = -j\omega\mu_0 \int \bar{\mathbf{G}}^b(\mathbf{r}', \mathbf{r}_{\mathrm{rec}})\mathbf{J}d^3\mathbf{r}', \tag{2.8}$$

where the integration is over the source volume.

Once $\mathbf{A}$ and $\mathbf{b}$ are formed, then the system may be solved for an estimate for the unknown contrast $\mathbf{x}$, a step commonly referred to as the *inverse solution*. In general, there will be many more unknown elements of $\mathbf{x}$ then there are channel measurements. The system of linear equations is ill-posed and underdetermined, and thus requires a regularized optimization technique to find a proper solution. Regularization puts constraints on the inversion in order to force the solution to have certain favorable qualities, which helps avoid convergence to an incorrect solution. This often takes the form of penalizing solutions with a large L_2 norm. An example of an inverse solution, which will be used for the studies in the following chapters, is conjugate gradient least squares (CGLS), an iterative solver that is regularized by termination prior to convergence.

After an estimate for the dielectric contrast, $\hat{o}(\mathbf{r}')$, is found, it is used to update the background profile. The background profile for DBIM iteration $i+1$ is thus given by $\varepsilon^*_{b(i+1)}(\mathbf{r}') = \varepsilon^*_{b(i)}(\mathbf{r}') + \hat{o}(\mathbf{r}')\varepsilon_0$. The DBIM iterates between forward and inverse solutions until convergence in the scattered field is achieved.

2.4 Conclusion

Microwave imaging for the breast is promising due to its ability to differentiate between high-density and low-density tissue. The ill-posed nature of inverse scattering remains a significant challenge. Existing techniques may be significantly improved by making them less sensitive to noise, interference, and model error. Such improvements can be algorithmic in nature, such as introducing transmit-receive beamforming. They can also be hardware based, such as introducing a fully-enclosed imaging environment and using efficient miniaturized antennas. The work to be done to incorporate these techniques will be both computational and experimental. The following chapters describe research completed towards accomplishing these important goals.

Chapter 3

Quantitative Microwave Imaging of Realistic Numerical Breast Phantoms Using an Enclosed Array of Multi-band, Miniaturized Patch Antennas

3.1 Introduction

In order to fully realize the benefits of microwave imaging for the breast, it is critical to use antenna arrays designed with the goal of counteracting the ill-posed nature of the linear system that must be solved as part of the imaging algorithm. This means using antennas with a small physical footprint, allowing for dense spatial sampling of electric fields. It also requires antennas that can collect electric fields at multiple discrete frequencies in the range 0.5 - 3.5 GHz. This frequency range balances the increased penetration depth and stabilizing effects of low frequencies [16] with the higher resolution from higher frequencies. Lastly, it is necessary to isolate the imaging region from the outside environment so that the measured electric fields are not corrupted by interference or clutter that can't be modeled in the forward solver.

The above requirements may be met through the use of electrically small dipoles, monopoles, or simple patches. These types of antennas may be impedance matched across a wide band of frequencies (thus allowing for multiple-frequency data to be collected) by immersing them in a lossy medium. The loss of the medium may also significantly attenuate signals from clutter outside

This chapter is partially adapted from M. Burfeindt, N. Behdad, B. Van Veen, and S. Hagness. "Quantitative Microwave Imaging of Realistic Numerical Breast Phantoms Using an Enclosed Array of Multi-band, Miniaturized Patch Antennas," *IEEE Antennas and Wireless Propagation Letters*, vol. 11, pp. 1626 - 1629.

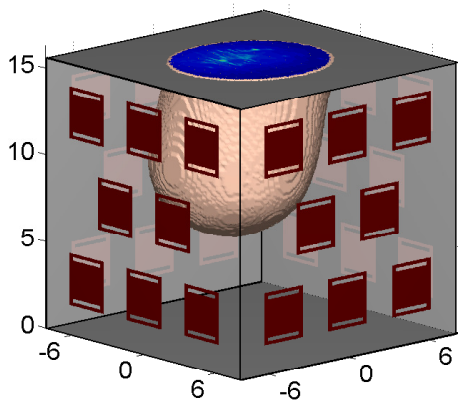

Figure 3.1: An illustration of a 32-element antenna array enclosing a Class 2 numerical breast phantom. The substrates and ground planes on the four lateral panels are not shown to enable visualization of the interior. Axes are in centimeters.

the imaging region. However, this is done at the cost of decreasing the efficiency of the antennas and greatly attenuating signals that travel the entire span of the array, which perhaps leads to a loss of valuable scattered field data. There is thus interest in using antenna arrays that accomplish dense spatial sampling, multiple frequency operation, and imaging region isolation by other means.

Fig. 3.1 shows our proposed array of multi-band, miniaturized patch antennas surrounded by a conducting enclosure. The breast of the prone patient extends through the opening in the top panel of the array. An enclosed configuration is attractive, as it shields the imaging environment from outside interference and clutter. This shielding also simplifies the model of the array environment in the forward solution of the imaging algorithm. A few single-frequency enclosed arrays have been reported (e.g., [66, 67]); however, the slot-loaded patch antennas composing our array are designed to radiate at multiple resonant frequencies within the range relevant to microwave breast imaging while maintaining a relatively small physical footprint and thus a dense source population [68]. Arrays using this type of antenna are relatively straightforward to model on a Cartesian grid, which further simplifies the forward solution.

The proposed array fits within the interstitial space of an MRI patient-support platform and thus also allows for co-registration of microwave breast images with MRI [18]. This setup, together with a tissue-immobilizing thermoplastic mesh [69], allows microwave data to be acquired immediately following an MR scan while the breast remains stationary. This configuration permits a rigorous validation of microwave imaging as a viable clinical tool for breast imaging.

While the factors above highlight the advantages of our approach, it is important to validate imaging feasibility prior to clinical imaging trials. In this chapter, we report a computational study of microwave imaging with our proposed array. Simulated electric field data is acquired for heterogeneous, anthropomorphic testbeds of known dielectric distributions–namely, four MRI-derived numerical breast phantoms ranging in density from mostly fatty to extremely dense. We show that the reconstructed dielectric profiles are very faithful to the true dielectric profiles of the phantoms. This successful imaging of anatomically realistic breast phantoms demonstrates the feasibility of microwave breast imaging using an enclosed array of miniaturized, multi-band patch antenna.

3.2 Antenna array

The microwave antenna array used in this study is in the form of a rectangular cavity. Conducting ground planes enclose the cavity on six sides. The ground plane of the top panel has an elliptical hole through which the pendant breast phantom descends. This hole conforms to the base of each breast phantom. The interior sides of the four lateral panels are coated with a 60 mil substrate with dielectric properties $\varepsilon_r = 6.15$ and $\sigma = 2.1$ mS/m. These properties are similar to those of Rogers RO4360 substrate.

The interior volume of the enclosed array is filled with an immersion medium whose dielectric properties are given by the Debye model parameters $\varepsilon_\infty = 2.24$, $\Delta\varepsilon = 0.73$, $\sigma_s = 0$, and $\tau = 5$ ps. This Debye model is similar to the dielectric dispersion of the biocompatible immersion medium of safflower oil over the frequency range 0.5 - 3.5 GHz [68].

Each of the four lateral array panels is populated with an eight-element sub-array of slot-loaded patch antennas. The slot-loading approach is similar to that presented in [70]. The antennas are

arranged in three rows, in a staggered 3-2-3 configuration that reduces the mutual coupling between vertically adjacent antennas [18, 71]. Vertical spacing and horizontal spacing between antennas (center-to-center) are both 48 mm. The patch antennas are of height 30 mm and width 28 mm. Slots are placed 2 mm from both radiating (i.e., top and bottom) edges of the patch antenna. The dimensions of the slots are 24 mm by 2 mm. The function of the slots is to move the lowest three transverse magnetic (TM) resonances of the antenna into the frequency range 0.5 - 3.5 GHz while maintaining a relatively small antenna footprint. The antenna feed is offset from the center of the patch by 3 mm in the vertical direction. The first three resonances of the antenna are at 1.6, 2.2, and 3.0 GHz. These resonances correspond to the TM_{100}, TM_{200}, and TM_{300} modes of the antenna, respectively. Note that the patch antenna has vertical polarization in these three modes. We determined the resonant frequencies of the antenna via finite-difference time-domain (FDTD) simulation.

3.3 Data acquisition simulation

The heterogeneous, anthropomorphic numerical breast phantoms used in this study are derived from MR scans of human subjects as described in detail in [1] (see [57] for modifications). We use one phantom from each of the four breast density classes as defined by the American College of Radiology, ranging from Class 1, or mostly fatty, to Class 4, or extremely dense.

Data acquisition is performed by simulating each numerical testbed via FDTD formulated for simulating dispersive media described by single-pole Debye models, as in [57]. FDTD simulations are performed using the Acceleware FDTD library (Acceleware, Calgary, Alberta, Canada.) We use three grid cells to capture the thickness of the substrate. A graded mesh is used to increase the grid discretization to 1 mm in the interior of the array. Using this grid, the transverse features of the patch antennas, as well as the breast phantom features, are modeled with a 1-mm discretization. The side and bottom boundaries of the computational domain are terminated with perfectly electrically conducting (PEC) planes. The top of the domain is terminated with a convolutional perfectly matched layer (CPML) absorbing boundary. An eight-cell buffer region is introduced between the CPML boundary and the PEC cap at the top of the array. The breast phantom is extended upwards

through the elliptical hole into the eight-cell buffer region. The rest of the buffer is filled with free space.

The 32 antenna feeds are modeled as one-cell-long lumped-element resistive voltage sources. The resistive voltage sources occupy the substrate grid cell closest to the ground plane. Two cells of PEC are used to connect each voltage source to the patch surface.

Each source sequentially transmits a modulated Gaussian pulse with a bandwidth covering 0.5 to 3.5 GHz. The resulting time-domain electric fields are recorded at all antenna feeds and converted to phasor form at the TM_{100}, TM_{200}, and TM_{300} resonant frequencies of the patch antennas via discrete Fourier transform.

3.4 Imaging technique

Estimates of the dielectric profiles of the numerical breast phantoms are computed using the multi-frequency, Debye parameter formulation of the distorted Born iterative method (DBIM) [58] as described in Chapter 2 and [57]. The forward solution is computed via FDTD on the same grid as was used for data acquisition. We avoid the inverse crime by adding Gaussian white noise to the simulated array measurements at a level corresponding to a signal-to-noise ratio (SNR) of 30 dB. SNR is defined here as the ratio between the total received signal power across all channels to the total noise power across all channels. As in [57], the inverse solution is constrained via the projected restart method such that the reconstructed Debye parameters are roughly proportional. We use the scalar formulation of the algorithm, in which the scattered electric field, incident electric field, and dyadic Green's function are replaced with their corresponding co-polarized (in this case, vertical) components. The scalar approximation is only used for the purposes of the imaging algorithm; all FDTD simulations compute the full vector field quantities.

The DBIM requires computation of the heterogeneous background Green's function at each iteration of the algorithm. We calculate the Green's function from the incident field (which is computed in the forward solution of the algorithm) via the relationship

$$G^b(\mathbf{r}) = \frac{-jR_s E^i(\mathbf{r})}{\omega\mu_0 \ell_s v_s}, \tag{3.1}$$

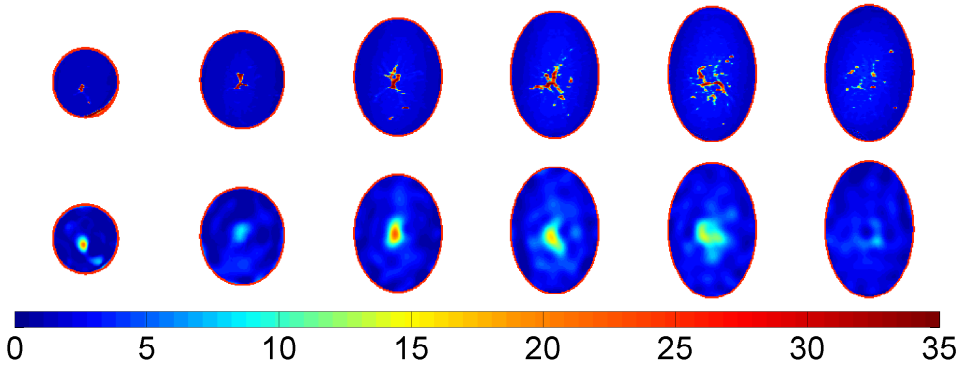

Figure 3.2: Class 1 (mostly fatty) phantom: Coronal cross-sections through the true (top row) and reconstructed (bottom row) profiles for the Debye parameter $\Delta\varepsilon$. Adjacent cross-sections are separated vertically by 2 cm.

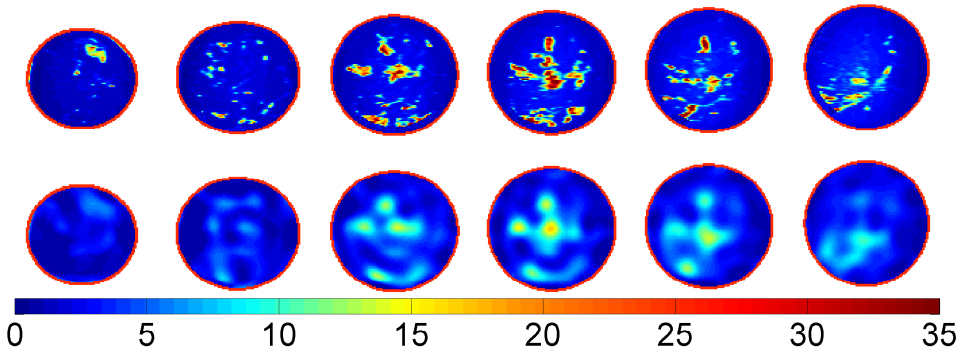

Figure 3.3: Class 2 (scattered fibroglandular) phantom: Coronal cross-sections through the true (top row) and reconstructed (bottom row) profiles for the Debye parameter $\Delta\varepsilon$. Adjacent cross-sections are separated vertically by 1 cm.

where E^i is the FDTD-computed incident electric field, G^b is the Green's function, ℓ_s is the length of the lumped element resistive voltage source, v_s is the source voltage phasor, and R_s is the source resistance. The computed Green's function takes into account multiple scattering within the enclosed array, as well as the characteristics of the antennas.

It is assumed that the dielectric properties of the breast voxels in the buffer region are unknown at each iteration of the DBIM algorithm. When the background profile is simulated in the forward solution, the row of voxels at the base of the breast phantom background profile is extended into the buffer region. The rest of the buffer region is again filled with free space.

As in [57], the imaging region in this study comprises all points interior to the phantom skin layer; thus, the skin is assumed known and is part of the background profile. Techniques have been developed for creating estimates of the breast surface using microwave backscatter measurements [72], and the dielectric properties of skin are well-characterized [73]. The initial guess in the phantom interior is homogeneous with dielectric properties corresponding to the volumetric mean of the exact profile.

The inverse solution is performed via conjugate-gradient least-squares (CGLS). Regularization is achieved by terminating CGLS after five conjugate gradient iterations. The DBIM is terminated when the norm of the residual vector $\mathbf{b}$ has changed by less than one percent of the initial residual norm, which occurs after five or six DBIM iterations.

3.5 Results and discussion

Figs. 3.2-3.5 show sequences of coronal cross-sections through the true and estimated 3-D dielectric profiles for each phantom. In each case, the profiles are depicted in terms of Debye parameter $\Delta\varepsilon$. The three Debye parameters are highly correlated in both the true and estimated profiles, so ε_∞ and σ_s are not shown. Adjacent cross-sections are separated vertically by 2 cm for the Class 1 phantom (the largest of the four phantoms) and 1 cm for Class 2 through Class 4.

The reconstructed profile is visually faithful to the true profile for each phantom. The low-level dielectric properties in the reconstructions correspond to fatty tissue. The reconstructed fibroglandular regions of tissues are accurate in location and basic shape. As in studies using idealized dipoles or line sources, the resolution is limited by the highest frequency used for the reconstruction. This contributes to the moderate blurring and underestimation of fibroglandular tissue dielectric properties in the reconstructions.

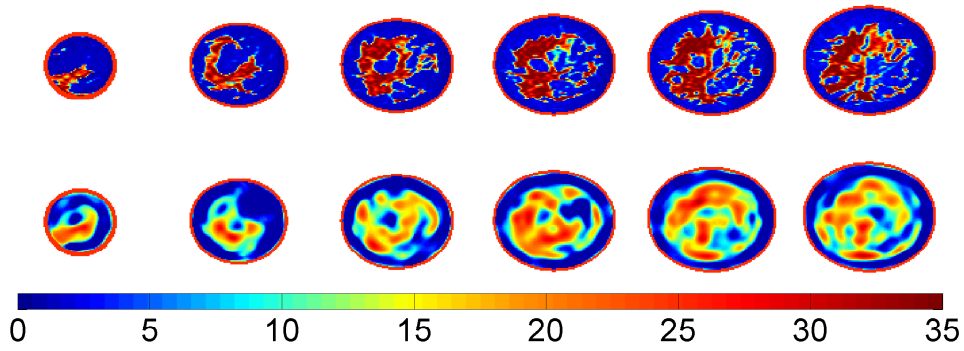

Figure 3.4: Class 3 (heterogeneously dense) phantom: Coronal cross-sections through the true (top row) and reconstructed (bottom row) profiles for the Debye parameter $\Delta\varepsilon$. Adjacent cross-sections are separated vertically by 1 cm.

We also report results in terms of the performance metric $\cos(\phi)$ introduced in [57], where ϕ is the angle between the true permittivity vector describing V and the corresponding estimated permittivity vector. Let $\mathbf{r}'_1 \ldots \mathbf{r}'_K$ be the locations of the K voxels in the imaging domain. Let the $3K \times 1$ vector $\mathbf{y}$ be the true permittivity vector, given by

$$\mathbf{y} = [\varepsilon_\infty(\mathbf{r}'_1) \ldots \varepsilon_\infty(\mathbf{r}'_K) \;\; \Delta\varepsilon(\mathbf{r}'_1) \ldots \Delta\varepsilon(\mathbf{r}'_K) \;\; \sigma_s(\mathbf{r}'_1) \ldots \sigma_s(\mathbf{r}'_K)]^{\mathrm{T}} \tag{3.2}$$

and let $\hat{\mathbf{y}}$ be the corresponding estimated permittivity vector. Then,

$$\cos(\phi) = \frac{\mathbf{y}^{\mathrm{T}}\hat{\mathbf{y}}}{||\mathbf{y}||_2||\hat{\mathbf{y}}||_2} \tag{3.3}$$

The quality metric quantifies the similarity in spatial distribution of dielectric properties between the actual and reconstructed profiles. A perfect reconstruction would have $\cos(\phi) = 1$. For this study, we obtained $\cos(\phi) = 0.8157$, 0.8408, 0.7972, and 0.7447, for the Class 1, 2, 3, and 4 phantoms, respectively. These values are comparable to the performance metrics for the reconstructions created by Shea, et al. using an idealized dipole array (see Fig. 8 in [57]). The somewhat diminished accuracy for the denser classes (3, 4) is likely due to higher attenuation associated with an increased percentage of fibroglandular tissue.

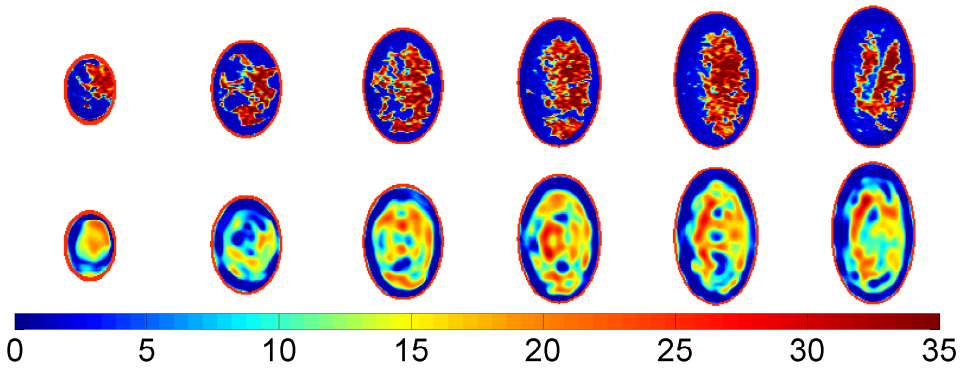

Figure 3.5: Class 4 (extremely dense) phantom: Coronal cross-sections through the true (top row) and reconstructed (bottom row) profiles for the Debye parameter $\Delta\varepsilon$. Adjacent cross-sections are separated vertically by 1 cm.

The optimal choices for substrate, slot-loaded patch antenna, resonant frequencies, and configuration of antennas in each sub-array remain open questions. Potential improvements could be realized by using a slot-loaded patch antenna with more resonant frequencies in the 0.5-3.5 GHz range, though this may result in a loss of gain. Alternate array configurations may affect the radiation pattern inside the cavity, possibly leading to further performance improvement.

3.6 Conclusion

This study presents results of imaging anatomically-realistic, MRI-derived numerical breast phantoms using an enclosed array of miniaturized patch antennas and a 3-D, multi-frequency formulation of the distorted Born iterative method. Visual qualitative agreement between the true phantom profiles and the 3-D reconstructed profiles is evident in all coronal cross-sections for all four phantom density classes. The performance metric $\cos(\phi)$ for each reconstruction is comparable to the corresponding metric for the idealized dipole array reconstructions despite using fewer and higher frequencies. Thus, an enclosed array of multi-band patch antennas has excellent potential for microwave breast imaging.

Chapter 4

The Prototype Microwave Imaging Array: Experimental Data Acquisition and Model Error Characterization

4.1 Introduction

The promising numerical results from the preceding chapter motivate development of an experimental microwave imaging prototype. Experimental microwave imaging via inverse scattering poses the additional challenge of mismatch between the true propagation environment in the antenna array and the simulated propagation environment of the forward solution. Sources of such model error include numerical dispersion, imperfect array construction, and ambiguity in the dielectric properties of the immersion medium. With such imperfections present, the difference between the measured and simulated received electric fields $E^s = E^t - E^i$ will contain an additional unwanted signal error that is distinct from noise or external interference. The imaging algorithm will attempt to compensate for this error, leading to aberrations in the resulting dielectric reconstruction. The magnitude of these aberrations will depend on the severity of the model error.

In this chapter, we characterize an experimental microwave imaging array of the type introduced in Chapter 3. The procedure for performing an experimental data acquisition and calibrating the resulting measurements is described. We then quantify the signal error between measurement and simulation of the array filled only with the immersion liquid. We then perform a sensitivity

This work was performed in collaboration with J. Shea, T. Colgan, R. Mays, N. Behdad, B. Van Veen, and S. Hagness.

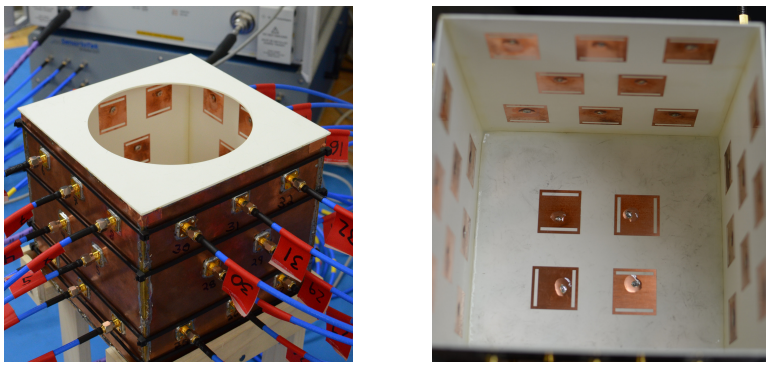

(a) **(b)**

Figure 4.1: Photographs of the enclosed array of patch antennas. a) An exterior view. b) An interior view, prior to attachment of the top panel. The safflower oil immersion isn't present for visualization purposes.

analysis, wherein we perturb various array parameters in simulation and quantify the degree to which it changes the resulting array signals. This sensitivity analysis helps us to identify features of the array which are most likely to introduce error into array signals.

4.2 The Prototype array and data acquisition system

Fig. 4.1a is a photograph of the prototype array of miniaturized, multi-band patch antennas. As in Chapter 3, the array consists of 30 mm high by 28 mm wide slot-loaded patch antennas. Slots of size 26 mm wide by 2 mm high are placed 2 mm from each radiating edge. The antenna feed is located 5 mm vertically off-center. There are a total of 36 patch antennas in the array. Each lateral panel is of size 156 mm high by 164 mm wide. These dimensions would allow the array to accommodate a majority of human subjects, based on the distributions of breast dimensions given in [74]. Each panel has a sub-array of eight antennas arranged in a 3-2-3 configuration. Antenna horizontal spacing is 48 mm, center-to-center. Vertical spacing is 46 mm between the bottom and middle rows and 48 mm between the middle and top rows. The bottom panel has a sub-array of four antennas, as pictured in Fig. 4.1b. Each array panel is formed from 60 mil (about 1.524 mm) Rogers RO4360 substrate backed by copper. The top array panel has a hole of diameter 125 mm.

For data acquisition, we fill the array with the biocompatible immersion medium of safflower oil. This immersion medium is convenient in that it decreases the dielectric contrast of the imaging object with the propagation medium of the array while also closely matching the dielectric properties of conformable thermoplastic mesh that will be used in clinical trials [69]. This match in properties obviates the need for accounting for the thermoplastic mesh in the forward solution of the imaging algorithm.

Data acquisition is performed via an Agilent two-port E8364A programmable network analyzer (PNA). The PNA interfaces with the antenna array through a 2×36 switch. The two PNA ports are connected to the input ports of the switch, while the switch output ports are connected to the antenna terminals via 36 secondary cables. Data acquisition automation is accomplished via LabView. For each transmit-receive antenna pair, the PNA outputs the 2×2 scattering matrix, i.e., the S-parameters of the antenna pair. The components of a scattering matrix are given by

$$S_{ij} = \left. \frac{v_i^-}{v_j^+} \right|_{v_{i \neq j}^+ = 0}, \tag{4.1}$$

that is, the ratio of the outgoing voltage wave from the ith port to the incoming voltage wave at the jth port, assuming there is no incoming voltage waves at any other ports. For this study, as well as for the imaging studies in the following chapters, we will be concerned with the bistatic antenna channels, wherein the transmitting antenna is distinct from the receive antenna. The bistatic signals are given by the off-diagonal S-parameters.

The two PNA terminals are calibrated to the input ports of the switch. The measured S-parameters thus include signal contributions from the switch paths and the secondary cables, which is undesirable. Removing the effects of the switch paths and the secondary cables is made more convenient by converting from a scattering matrix formulation to a transmission matrix formulation, as transmission matrices for different hardware components of the data acquisition system can be cascaded together in order to represent the transmission matrix for the system as a whole. This cascading technique makes it relatively simple to remove the effects of the unwanted components from the signal before converting back to a scattering matrix formulation.

For a given antenna pair, the PNA-measured scattering matrix can be converted into a 2×2 transmission matrix, T_{PNA}, and vice-versa via a set of simple relations [75]. The transmission matrix between the feeds of the antennas, T_{antennas}, can then be related to T_{PNA} via the simple equation

$$T_{\mathrm{antennas}} = B_2^{-1} T_{\mathrm{PNA}} B_1^{-1}. \tag{4.2}$$

where B_1 is the transmission matrix between the first switch input and the output of the secondary cable connected to the first antenna and B_2 is the transmission matrix between the second switch input and the output of the secondary cable connected to the second antenna. We determine B_1 and B_2 for each antenna pair by first measuring the S-parameters for every switch path and secondary cable via the PNA. We then remove the signal contributions from the switch and secondary cables by applying (4.2) to the PNA measured signal for each antennas pair. The effective S-parameters between the two antenna terminals, free of the effects of the cables or switch paths, are then computed by application of the relations from [75] to T_{antennas}.

4.3 Simulation of the antenna array

The prototype array is simulated via FDTD in the manner described in Chapter 3. A two-pole Debye model of the form in (2.1) is used to model the dispersive dielectric properties of the safflower oil, with parameters $\varepsilon_\infty = 2.35$, $\Delta\varepsilon = 0.33$, $\sigma_s = 0$, $\tau_1 = 20$ ps, and $\tau_2 = 202$ ps. This model closely matches the dispersion of safflower oil measured with the Agilent 85070 high-temperature probe.

A one-grid-cell layer of substrate is placed above the top PEC layer in order to model the substrate on the top array panel. The slight mismatch (1 mm versus 1.524 mm) in the simulated versus experimental thickness of the substrate of the top panel is assumed to provide negligible corruption of the forward solution signal, as the interior of the array is shielded from reflections from the substrate by the conductor of the top panel. Modeling the top panel in this manner allows us to avoid grading the FDTD mesh vertically into the array hole, which would require non-uniformly sized imaging region voxels.

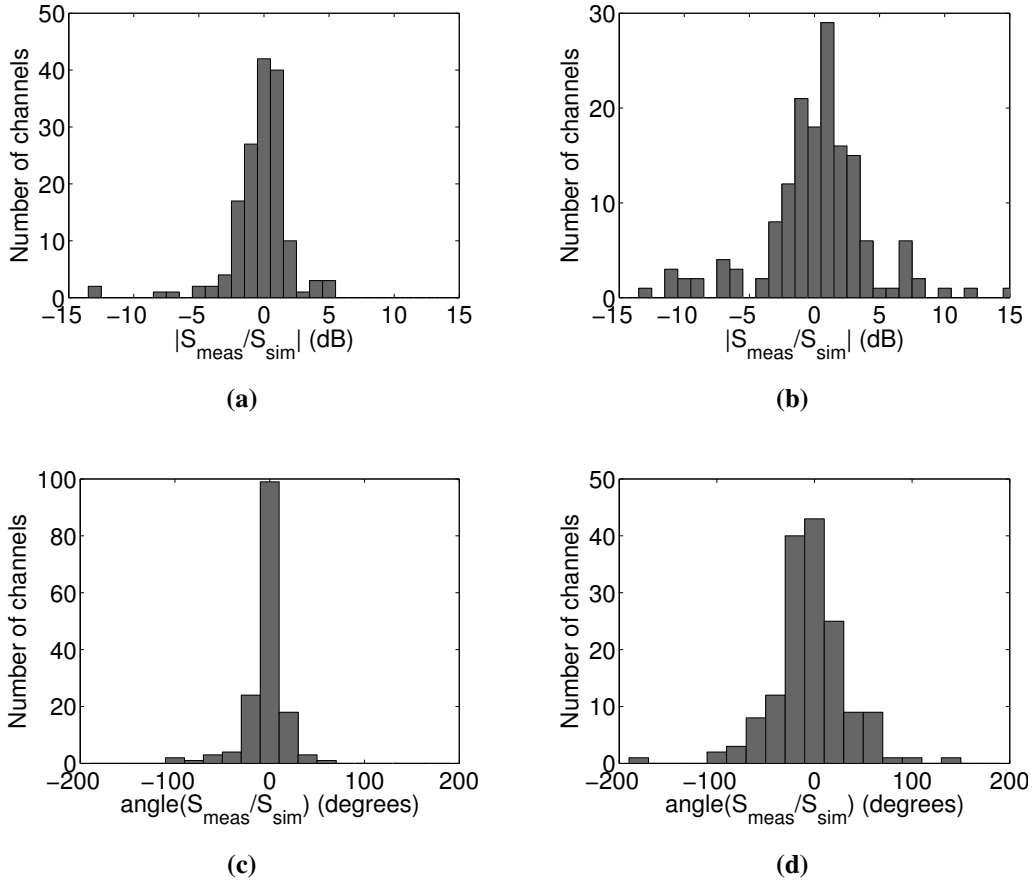

Figure 4.2: Histograms for (a)-(b) magnitude and (c)-(d) angle errors between experiment and measurement. Left column: 1.61 GHz. Right Column: 3.06 GHz. The histogram in (b) neglects an outlier channel with an error of 24 dB.

The simulation is terminated after 40 ns of simulation time, after which the received time-domain voltages have decayed to about -40 dB referenced to their peak. The received time-domain simulated voltages at all antenna feeds are converted to frequency-domain via DFT. Bistatic scattering matrix parameters can be calculated from the current and voltage phasors at each port using the relations given in [76]. For the case where the source port is excited by a matched resistive voltage source and all receiving ports are terminated with a matched load, these relations reduce to

$$S = 2v/v_s, \tag{4.3}$$

where v is the voltage phasor recorded at the antenna feed in question and v_s is the source voltage phasor. For a system not excited by a resistive voltage source, v_s is the Thevenin equivalent voltage source at the source port. We use (4.3) to convert the simulated voltage phasors at each port to S-parameters.

4.4 Results and discussion

We first compare the measured and simulated S-parameters for the prototype array in order to compute the degree of model error in the forward solution. An angle offsets exists between experimental and simulated S-parameter phasors at each frequency, most likely due to stray uncompensated electrical lengths from connectors. We correct for this effect by subtracting the median angle offset across channels from the measured phasors. Fig. 4.2 shows histograms for the magnitude and phase errors between measurement and simulation. The histograms include channels formed by transmitting with five antennas on one panel and receiving with all 32 antennas on the four lateral panels. The five transmit antennas are chosen so that all geometrically unique channels on the lateral panels are included. A magnitude and phase histogram is shown for both the TM_{100} resonance at 1.61 GHz and the TM_{300} resonance at 3.06 GHz. For the lower band, 90% of the channels have a magnitude error of less than 3 dB, and 91% have a phase error of less than 30 degrees. For the upper band, 67% have a magnitude error of less than 3 dB, and 70% have an angle error of less than 30 degrees.

The overall degree of model error may also be quantified using the perturbation metric

$$\gamma = \frac{|S|}{|S - S_0|}, \tag{4.4}$$

where S is the perturbed (in this case, measured) signal phasor and S_0 is a baseline (in this case, simulated) signal. The metric γ is akin to a signal-to-noise ratio (SNR), where the denominator is the perturbation in signal due to model error as opposed to noise. For the lower band, $\gamma = 15$ dB for the median channel, while for the upper band, $\gamma =$7 dB. This is consistent with the histograms in Fig. 4.2. The degree of model error is considerably greater for the upper frequency band than for the lower frequency band. These results suggest that the upper frequency band is more sensitive to

small imperfections in array construction or ambiguities in dielectric properties of array materials. The higher degree of model error in the higher frequency band suggests that creating accurate multi-band reconstructions will require emphasizing the lower frequency data more in the inverse system.

Assuming a conservative noise floor of -70 dB referenced to source power and a median received signal at around -30 dB, a median SNR of 40 dB is a reasonable estimate for an experimental microwave data acquisition system. Based on the signal-to-model-error ratios given by the metric γ above, the corruption of the scattered field signal due to model error is more pernicious than instrument noise by several orders of magnitude. This suggests that model error is among the most important challenges in experimental microwave imaging.

We also perform a sensitivity analysis in order to identify which features of the array are most likely to cause mismatch between measurement and forward solution if perturbed. We make a series of small changes to the simulated antenna array and compare the resulting simulated signals to the baseline simulated signals. The metric γ is then reported, where S is considered to be the signal from the perturbed simulation and S_0 is the signal from the baseline simulation. For perturbations that resulted in a small shift in resonant frequency of the antenna, such as changing dielectric properties of materials in the array, we sample S at the perturbed resonance and S_0 at the unperturbed resonance.

Table 4.1 lists the various perturbations included in this study. The perturbation of ± 0.15 was chosen for the substrate dielectric constant in order to match the reported tolerances for the Rogers substrate. Perturbations of 2 mm for the panel dimensions and 10 mm for the hole diameter were chosen to represent larger than expected aberrations. For perturbation 17, the lateral boundaries of the computational domain were changed to CPML from PEC. A buffer of 5 cells was placed between the CPML and the lateral ground planes on all sides. This change was made so that there were no lateral PEC planes above the array top cap, which corresponds to the experimental setup. For perturbation 18, the substrate above the top panel was changed in thickness from 1 to 1.5 mm. The FDTD grid was graded vertically into the hole in order to accomplish this. A perturbation of 10% was chosen for the rest of the features.

Table 4.1: List of perturbations for the sensitivity analysis and resulting γ for the median channel

Perturbation number	Description	γ (dB) TM_{100}	γ (dB) TM_{300}
1	Increase substrate dielectric constant from 6.15 to 6.3	24	35
2	Decrease substrate dielectric constant from 6.15 to 6.0	24	35
3	Increase substrate conductivity by 10%	23	21
4	Decrease substrate conductivity by 10%	24	21
5	Increase panel width by 2 mm	27	20
6	Decrease panel width by 2 mm	27	20
7	Increase panel height by 2 mm	27	19
8	Decrease panel height by 2 mm	27	20
9	Increase hole diameter by 10 mm	23	17
10	Decrease hole diameter by 10 mm	23	18
11	Decrease grid sample spacing to 0.5 mm	20	29
12	Increase grid sample spacing to 2 mm	17	17
13	Increase oil dielectric constant by 10%	14	10
14	Decrease oil dielectric constant by 10%	14	9
15	Increase oil conductivity by 10%	23	22
16	Decrease oil conductivity by 10%	22	21
17	Remove lateral PEC boundaries above top plate	22	21
18	Model substrate of top panel with 1.5-mm thickness	52	36

Table 4.1 also gives the results of the sensitivity study for both the TM_{100} and TM_{300} frequency bands. For most perturbations, γ was around 20 dB or more, signifying that the signal was relatively insensitive to most aberrations in array feature dimensions or dielectric properties. The signal was particular insensitive to the thickness of the substrate above the top panel and (for the upper frequency) lateral substrate dielectric properties. The signal was most significantly changed

when the permittivity of the oil immersion was perturbed. This is most likely because the signal undergoes progressively larger change as it travels across the width of the antenna array in a slightly different immersion medium. Signal changes were generally greater for the higher frequency band. This result is consistent with the higher frequency band being more sensitive to small construction errors.

4.5 Conclusion

This chapter introduced the experimental prototype enclosed array of miniaturized, multi-band patch antennas. The experimental data acquisition process was described, as well as the process for acquiring simulated scattering matrix parameters. These two techniques will be used in the proceeding two chapters for experimental imaging with the prototype array. A comparison between simulation and measurement showed a significantly higher degree of model error for the TM_{300} mode as opposed to the TM_{100} mode of the antenna, suggesting that higher frequencies are more easily corrupted by imperfections in array construction or ambiguities in dielectric properties. For both bands, the signal perturbation caused by model error is significantly larger than what would be expected due to instrument noise alone, which suggests that model error is among the most significant challenges for microwave breast imaging. A sensitivity study in which we perturbed various features of the simulated array suggested that the array is moderately insensitive to small errors in array feature dimensions and very sensitive to errors in the dielectric properties of the immersion medium.

Chapter 5

Preliminary Experimental Imaging of Simple Objects with the Prototype Array

5.1 Introduction

This chapter reports the results of reconstructing the dielectric profiles of a series of simple objects based on experimental data acquisition using the enclosed array of miniaturized, multi-band patch antennas described in Chapter 4. These imaging cases allow the evaluation of the ability of the imaging system to reconstruct the dielectric profiles for targets of varying size and configuration. Successful experimental imaging of simple objects also provide a baseline with which to judge the effectiveness of experimentally imaging more complex or anatomically realistic domains.

The following section describes the geometrically simple test objects used in this study. The method of applying experimental data to the imaging algorithm is then given in detail, including the reformulation of the scattered field integral equation for measured scattering matrix parameters and modifications to the algorithm for overcoming the corrupted nature of the scattered signals caused by noise or model error. The reconstructed profiles are then reported, with the result that each test object was accurately imaged in terms of the basic shape and location of its high-permittivity regions.

Sec. 5.2 is partially adapted from M. Burfeindt, T. Colgan, R. Mays, J. Shea, N. Behdad, B. Van Veen, and S. Hagness. "MRI-derived 3-D-printed Breast Phantom for Microwave Breast Imaging Validation," *IEEE Antennas and Wireless Propagation Letters*, vol. 11, pp. 1610 - 1623. [77]. The work in the remaining sections was also performed in collaboration with the same co-authors.

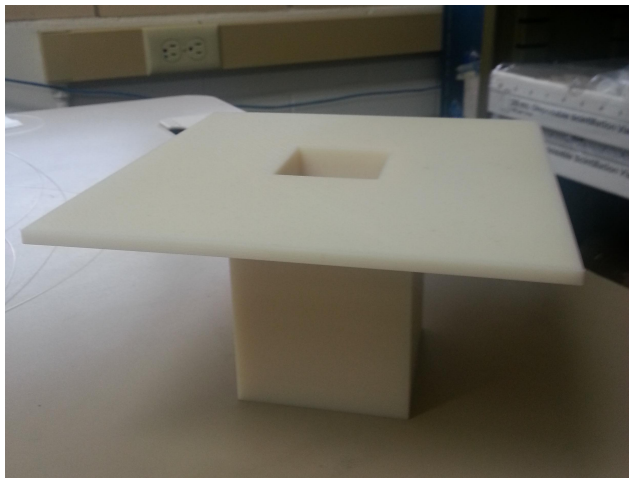

Figure 5.1: A photograph of the 3-D-printed square cylindrical phantom.

5.2 Phantoms for experimental data acquisition

The square cylinder phantom used in this study is composed of acrylonitrile butadiene styrene (ABS) plastic and is pictured in Fig. 5.1. It was printed using a Dimension Elite 3-D Printer (Dimension, Inc., Eden Prairie, MN) and has outer dimensions of $90 \times 70 \times 70$ mm. There is a void in the phantom into which a liquid can be poured in order to provide a high-contrast target within the plastic. The void is also in the shape of a square cylinder and has dimensions $80 \times 40 \times 40$ mm. There is a 5-mm-thick slab at the top of the phantom that is used to suspend it through the hole in the top panel of the antenna array.

Knowledge of the dielectric properties of the materials constituting the phantom is important for quantitative evaluation of the resulting microwave images. We characterized the dielectric properties of the 3-D-printed ABS plastic using the technique described in [69]. First, we 3-D-printed a slab of ABS plastic of dimensions $200 \times 100 \times 2$ mm. We then fabricated a microstrip transmission line of length 200 mm and width 6 mm on the plastic slab. SMA connectors were soldered to both ends of the transmission line and $S-$parameter measurements were made using an Agilent E8364 vector network analyzer. Agilent's commercial software package Advanced Design System (ADS) was then used to create a simulated microstrip transmission-line model. The permittivity and loss tangent of the simulated microstrip line were optimized in ADS at 0.5 GHz

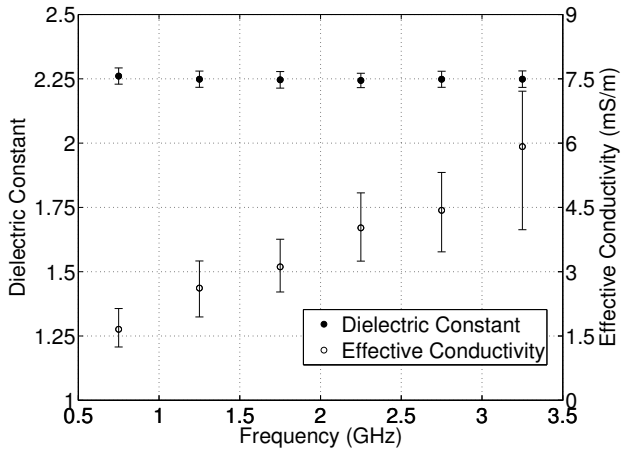

Figure 5.2: Measured dielectric constant and effective conductivity for 3-D-printed ABS plastic. © 2012 IEEE.

intervals to obtain a good match between simulation and measurement. The process was repeated for five different transmission lines. The resulting estimated dielectric constant and effective conductivity are plotted in Fig. 5.2 over the frequency range of interest for quantitative microwave breast tomography (0.5-3.5 GHz). Data points correspond to the mean over the five transmission lines and error bars span the maximum and minimum values. The dielectric constant is around 2.25 across the entire frequency range, while the effective conductivity ranges from a minimum of 1.7 mS/m at 0.75 GHz to a maximum of 5.9 mS/m at 3.25 GHz.

We fill the void of the 3-D-printed phantom first with Triton X-100 surfactant and then with a 90%-10% solution of glycerol and deionized water. The dielectric properties of these materials at the TM_{100} and TM_{300} frequency bands, as measured by the Agilent 805070 slim-form probe, are given in Table 5.1.

We also acquire data from suspended test tubes filled with 80%-20% solutions of glycerol and deionized water. The measured dielectric properties of 80%-20% glycerol-water solutions are also given in Table 5.1. Test tubes of two different sizes are used: 13 mm in diameter and 25 mm in diameter. The test tubes are suspended into the array by embedding them in a bridge of styrofoam

Table 5.1: Dielectric properties of glycerol-water solutions

Phantom material	ε_r, 1.6 GHz	ε_r, 3.0 GHz	σ_{eff} (S/m), 1.6 GHz	σ_{eff} (S/m), 3.0 GHz
Triton X-100	4.6	4.1	0.10	0.15
90% glycerol-10% water	10.7	8.1	0.9	1.0
80% glycerol-20% water	19.0	12.6	1.5	2.0

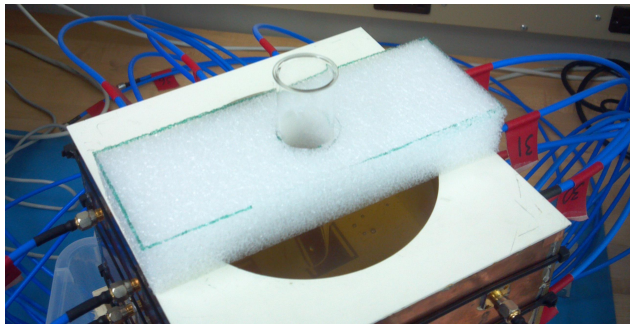

Figure 5.3: Experimental setup for data acquisition from a 25-mm test tube of 80% glycerol

that straddles the hole of the hole in the top array panel, as shown in Fig. 5.3. For both sizes, an 80-mm length of tube is allowed to descend into the array.

5.3 The Imaging algorithm applied to experimental data

For the experimental imaging case, the goal of the imaging algorithm is to reconstruct the dielectric profile of the imaging region based on the measured S-parameters. Following the nomenclature of Sec. 2.3, let the measured S-parameter phasor from a given transmit receive pair be $S^t(\mathbf{r}_{\text{src}}, \mathbf{r}_{\text{rec}})$, and let the corresponding S-parameter phasor resulting from simulating the background profile be $S^i(\mathbf{r}_{\text{src}}, \mathbf{r}_{\text{rec}})$. We can write the difference between these two phasors using (4.3) as

$$S^t(\mathbf{r}_{\text{src}}, \mathbf{r}_{\text{rec}}) - S^i(\mathbf{r}_{\text{src}}, \mathbf{r}_{\text{rec}}) = \frac{2v^t}{v_s} - \frac{2v^i}{v_s}, \tag{5.1}$$

where v^i is the simulated voltage phasor at the feed of the receiving antenna, v^t is the corresponding effective measured voltage phasor, and v_s is the source voltage phasor. For the incident field v_s

is the source phasor used in the forward solution, where for the total field v_s is the Thévenin equivalent for the source of the data acquisition system. The voltages may be converted to electric fields by multiplying by ℓ_s, the length of the lumped element resistor. This step assumes that the voltage measured by the data acquisition system is equivalent to the voltage that would be measured across a resistor of length ℓ_s across the antenna terminals. The S-parameter equivalent to the scattered field integral equation (2.2) can then be written using the scalar and Born approximations as

$$S^t(\mathbf{r}_{\rm src}, \mathbf{r}_{\rm rec}) - S^i(\mathbf{r}_{\rm src}, \mathbf{r}_{\rm rec}) = \frac{2\omega^2\mu_0\varepsilon_0\ell_s}{v_s}\int_V G^b(\mathbf{r}', \mathbf{r}_{\rm rec})E^i(\mathbf{r}_{\rm src}, \mathbf{r}')o(\mathbf{r}')d^3\mathbf{r}'. \tag{5.2}$$

Eq. (5.2) serves as the basis for the experimental imaging algorithm. The specifics of implementation of the experimental algorithm are given in the following subsections.

Application of a Window to the Forward Solution and Data Acquisition

The forward solution of the DBIM is performed in the manner described in Chapter 4. Due to the low-loss and resonant nature of the array cavity, many reflections occur in the antenna array before all electric fields dissipate. The most useful scattered field data occurs in the early reflections. Thus, we terminate the forward solution prior to complete dissipation of the recorded time-domain signals. This is equivalent to using a rectangular window in the time domain and convolving with a sinc window in the frequency domain. We accordingly apply the appropriate sinc window to the measured $S-$parameter data.

It is necessary to know the effect of the window on the integral equation in order to formulate the linear equation to be solved. The effect of the window can be determined by first considering the Helmholtz equation for the electric field $\mathbf{E}$ resulting from source current density $\mathbf{J}$

$$\nabla^2\mathbf{E}(\mathbf{r}') + \omega^2\mu_0\varepsilon^*\mathbf{E}(\mathbf{r}') = j\omega\mu_0\mathbf{J} \tag{5.3}$$

and the corresponding equation for the Green's function,

$$\nabla^2\mathbf{G}(\mathbf{r}', \mathbf{r}) + \omega^2\mu_0\varepsilon^*\mathbf{G}(\mathbf{r}', \mathbf{r}) = -\delta(\mathbf{r} - \mathbf{r}'), \tag{5.4}$$

where $\delta(\mathbf{r})$ is the Dirac delta distribution. Let W be the frequency domain sinc window, $\otimes$ denote frequency domain convolution, $\breve{\mathbf{E}} = W \otimes \mathbf{E}$, and $\breve{\mathbf{G}} = W \otimes \mathbf{G}$. Then, applying the sinc window

to (5.3) and (5.4) results in

$$\nabla^2 \breve{\mathbf{E}} + \omega^2 \mu_0 \varepsilon^* \breve{\mathbf{E}} = j\omega\mu_0 \breve{\mathbf{J}} \tag{5.5}$$

and

$$\nabla^2 \breve{\mathbf{G}} + \omega^2 \mu_0 \varepsilon^* \breve{\mathbf{G}} = -\delta(\mathbf{r} - \mathbf{r}'). \tag{5.6}$$

In (5.5) and (5.6), we have used the approximation $W \otimes \omega^2 \mathbf{E} \approx \omega^2 W \otimes \mathbf{E}$, or equivalently in the time domain $W(t)\frac{\partial^2}{\partial t^2}\mathbf{E}(t) \approx \frac{\partial^2}{\partial t^2} W(t)\mathbf{E}(t)$, which is a good approximation when $W(t)$ is a rectangular window. Multiplying (5.5) by $\breve{\mathbf{G}}$ and (5.6) by $\breve{\mathbf{E}}$ leads to

$$\breve{\mathbf{G}}\nabla^2 \breve{\mathbf{E}} + \omega^2 \mu_0 \varepsilon^* \breve{\mathbf{G}}\breve{\mathbf{E}} = j\omega\mu_0 \breve{\mathbf{G}}\breve{\mathbf{J}} \tag{5.7}$$

and

$$\breve{\mathbf{E}}\nabla^2 \breve{\mathbf{G}} + \omega^2 \mu_0 \varepsilon^* \breve{\mathbf{E}}\breve{\mathbf{G}} = -\breve{\mathbf{E}}\delta(\mathbf{r} - \mathbf{r}'). \tag{5.8}$$

Subtracting (5.7) from (5.8) and integrating over the entire volume gives

$$\begin{aligned} \int \breve{\mathbf{E}}\delta(\mathbf{r} - \mathbf{r}')d^3\mathbf{r}' &= \breve{\mathbf{E}}(\mathbf{r}) \\ &= -j\omega\mu_0 \int \breve{\mathbf{G}}\breve{\mathbf{J}}\, d^3\mathbf{r}' + \int \left(\breve{\mathbf{E}}\nabla^2\breve{\mathbf{G}} - \breve{\mathbf{G}}\nabla^2\breve{\mathbf{E}}\right) d^3\mathbf{r}'. \end{aligned} \tag{5.9}$$

The last integral in (5.9) can be set to zero using Green's second identity, leading to

$$\breve{\mathbf{E}}(\mathbf{r}) = -j\omega\mu_0 \int \breve{\mathbf{G}}\breve{\mathbf{J}}\, d^3\mathbf{r}'. \tag{5.10}$$

Using the volume equivalence theorem, the Helmholtz equation for the windowed scattered field can be written

$$\nabla^2 \breve{\mathbf{E}}^s + \omega^2 \mu_0 \varepsilon_b^* \breve{\mathbf{E}}^s = j\omega\mu_0 \breve{\mathbf{J}}_{\mathrm{eq}}, \tag{5.11}$$

where the equivalent current density is

$$\breve{\mathbf{J}}_{\mathrm{eq}} = j\omega\varepsilon_0 o(\mathbf{r}')\breve{\mathbf{E}}^t. \tag{5.12}$$

Using (5.10), (5.12), and the Born approximation, we are left with

$$\breve{\mathbf{E}}^s(\mathbf{r}) = \omega^2 \mu_0 \varepsilon_0 \int_V \breve{\mathbf{G}}^b(\mathbf{r}, \mathbf{r}')\breve{\mathbf{E}}^i(\mathbf{r}')o(\mathbf{r}')d^3\mathbf{r}', \tag{5.13}$$

which is equivalent to the Born-approximated (2.2) wherein the Green's function and incident field in the kernel are in their windowed form. The windowed Green's function may be written in terms of the windowed incident field via (5.10) in order to obtain the relation similar to (3.1), where the non-windowed quantities have been replaced with their windowed quantities. This step requires the approximation $\breve{\mathbf{J}} \approx \mathbf{J}$, which is valid assuming the time-domain span of the source function is shorter than the time-domain rectangular window. This analysis shows that the incident field at the antennas and the field quantities in the integral kernel can be computed and windowed simply by terminating the forward solution at the end of the rectangular window. In the following sections, use of a window will be assumed, and so the breve notation on windowed quantities will be neglected.

Linear system of equations

Eqs. (2.4) and (2.5) can then be written as

$$\mathbf{b} = \begin{bmatrix} \Re\left\{S^t(\mathbf{r}_{\mathrm{src}(1)}, \mathbf{r}_{\mathrm{rec}(1)}) - S^i(\mathbf{r}_{\mathrm{src}(1)}, \mathbf{r}_{\mathrm{rec}(1)})\right\} \\ \vdots \\ \Re\left\{S^t((\mathbf{r}_{\mathrm{src}(M)}, \mathbf{r}_{\mathrm{src}(M)}) - S^i(\mathbf{r}_{\mathrm{src}(M)}, \mathbf{r}_{\mathrm{src}(M)})\right\} \\ \Im\left\{S^t(\mathbf{r}_{\mathrm{src}(1)}, \mathbf{r}_{\mathrm{rec}(1)}) - S^i(\mathbf{r}_{\mathrm{src}(1)}, \mathbf{r}_{\mathrm{rec}(1)})\right\} \\ \vdots \\ \Im\left\{S^t(\mathbf{r}_{\mathrm{src}(M)}, \mathbf{r}_{\mathrm{src}(M)}) - S^i(\mathbf{r}_{\mathrm{src}(M)}, \mathbf{r}_{\mathrm{src}(M)})\right\} \end{bmatrix} \tag{5.14}$$

and

$$A^0_{mk} = \frac{2\Delta^3\omega^2\mu_0\varepsilon_0\ell_s}{v_s} G^b(\mathbf{r}'_k, \mathbf{r}_{\mathrm{rec}(m)}) E^i(\mathbf{r}_{\mathrm{src}(m)}, \mathbf{r}'_k). \tag{5.15}$$

All field and S-parameter quantities in (5.14) and (5.15) refer to the quantities obtained after applying the appropriate sinc window.

Two types of dielectric reconstructions are performed in this study. In the first, only frequencies from a single frequency band are used, and parameters ε_r and σ_{eff} for the frequency band of interest are reconstructed for each imaging region voxel. Eq. (2.6) is then written

$$\mathbf{A} = \begin{bmatrix} \Re\{\mathbf{A}^0\} & -\Im\{c_\sigma\}\Im\{\mathbf{A}^0\} \\ \Im\{\mathbf{A}^0\} & +\Im\{c_\sigma\}\Re\{\mathbf{A}^0\} \end{bmatrix}, \tag{5.16}$$

where c_σ has the same meaning as in Chapter 2. In the second case, frequencies from both the TM_{100} and TM_{300} mode are used, which requires a parameterized reconstruction. The materials to be imaged in this chapter can each be well-characterized using two-pole Debye models with $\sigma_s = 0$. Thus, we assume $\sigma_s = 0$ for all voxels in the imaging domain and reconstruct only Debye parameters ε_∞ and $\Delta\varepsilon$. Eq. (2.6) is then written as

$$\mathbf{A} = \begin{bmatrix} \Re\{\mathbf{A}^0\} & \Re\{c_\Delta\}\Re\{\mathbf{A}^0\} - \Im\{c_\Delta\}\Im\{\mathbf{A}^0\} \\ \Im\{\mathbf{A}^0\} & \Im\{c_\Delta\}\Re\{\mathbf{A}^0\} + \Re\{c_\Delta\}\Im\{\mathbf{A}^0\} \end{bmatrix}, \tag{5.17}$$

where $c_\Delta = 1/(1 + j\omega\tau_1) + 1/(1 + j\omega\tau_2)$. A reconstruction of this type requires that all materials in the imaging domain can be well-modeled using the same τ_1 and τ_2. As described in Chapter 2, the multiple-frequency linear system is created by forming $\mathbf{A}$ and $\mathbf{b}$ for each frequency and then vertically concatenating. For a reconstruction with F frequencies, let $\mathbf{b}'$ represent the $2MF \times 1$ multi-frequency residual vector and let $\mathbf{A}'$ represent the $2MF \times 2K$ multi-frequency $\mathbf{A}$ matrix.

Row and Column Weighting

We apply row and column weighting to the linear system in order to address challenges inherent to experimental imaging of the materials described above. Let $\mathbf{R}$ be a $2MF \times 2MF$ diagonal matrix, where the mth diagonal component represents the weight for the mth row. Likewise, let $\mathbf{C}$ be a $2K \times 2K$ diagonal matrix whose kth diagonal component is the weight for the kth column. The linear system can then be written

$$\mathbf{RA'xC} = \mathbf{RA'z} = \mathbf{Rb'C}, \tag{5.18}$$

where $\mathbf{z} = \mathbf{xC}$. An estimate $\hat{\mathbf{z}}$ is then solved for, allowing computation of the estimate for the unknown contrast $\hat{\mathbf{x}} = \hat{\mathbf{z}}\mathbf{C}^{-1}$.

We apply row weighting in this study to account for the higher degree of model error in the TM_{300} frequency band, as described in Chapter 4. The lower frequency band of the antenna is narrower than the higher band, which causes the lower band data to decrease more in amplitude than the upper band data following convolution with the sinc window. We first correct for this effect by setting the weight for each row to be equal to the inverse of S^t for the corresponding

channel. We then multiply the row weights for the frequencies in the upper band by a factor of 1/5. By applying row weights in this fashion, we force the inverse solver to give more emphasis to the less-corrupted lower frequency data while still allowing the upper frequency data to contribute useful higher spatial frequency data to the solution.

We apply column weighting to the system in order to keep the scaling of the ε_∞ and $\Delta\varepsilon$ parameters comparable. We choose the weights for columns corresponding to the $\Delta\varepsilon$ parameter to be the ratio between ε_∞ and $\Delta\varepsilon$ for the material of highest permittivity in the imaging region. Correcting for the differences in scale between the two Debye parameters leads to a better-behaved inversion.

The Inverse Solution

The linear system is constructed using three frequencies in each band chosen for the reconstruction. Thus, F=3 for a reconstruction using only the TM_{100} mode, and F=6 for a reconstruction using both the TM_{100} and TM_{300} modes. Previous studies have used multiple frequencies in a single band [78]. This practice allows us to partially overcome the greater-than-desired corruption of the scattered signals. The three frequencies chosen are centered at the resonant frequency for the band and separated by 20 MHz.

The inverse solution is performed on a Cartesian 2-mm basis; this coarser basis allows us to decrease the memory needed to solve the system of linear equations. Conjugate-gradient least-squares with five conjugate gradient iterations is once again used to solve the linear system. We use the projected restart algorithm in order to achieve a desired proportionality between the reconstructed Debye parameters at each imaging region voxel. Using this algorithm, the estimated Debye parameters for a multi-band reconstruction are constrained to closely match a linear relationship based on *a priori* knowledge of the Debye parameters of the two materials in the imaging region, such that

$$\alpha_0\beta\left(\varepsilon_\infty - \varepsilon_\infty^0\right) \leq \Delta\varepsilon \leq \alpha_1\beta\left(\varepsilon_\infty - \varepsilon_\infty^0\right). \tag{5.19}$$

In (5.19), β is the slope of the line constraining the relationship between $\Delta\varepsilon$ and ε_∞, given by

$$\beta = \frac{\Delta\varepsilon_1 - \Delta\varepsilon_2}{\varepsilon_{\infty,1} - \varepsilon_{\infty,2}}, \tag{5.20}$$

where $\Delta\varepsilon_1$ and $\Delta\varepsilon_2$ are the delta permittivities for the first and second materials in the imaging region, respectively, and $\varepsilon_{\infty,1}$ and $\varepsilon_{\infty,2}$ are similarly the infinite permittivities for the two materials. The parameter ε_∞^0 is the infinite permittivity corresponding to a delta permittivity of zero, given by

$$\varepsilon_\infty^0 = -\Delta\varepsilon_1/\beta + \varepsilon_{\infty,1}. \tag{5.21}$$

The parameters α_0 and α_1 determine how far the estimated parameters are allowed to deviate from the linear model. We choose $\alpha_0 = 0.8$ and $\alpha_1 = 1.2$. For a single-band reconstruction, (5.19)-(5.21) are reformulated for dielectric parameters ε_r and σ_{eff}.

Applying the projected restart algorithm using (5.19)-(5.21) requires knowledge of the Debye parameters for each material in the imaging region. Table 5.2 gives the assumed Debye parameters for each material used in this study. The parameters were chosen so that the resulting Debye models closely matched the dielectric dispersion measured with the Agilent 85070 slim-form probe high-temperature probe. For the case of imaging test tubes of glycerol solution, the safflower oil immersion is part of the imaging region and must therefore be reconstructed. The Debye parameters for the oil outside the imaging region are assumed to be the parameters given in the previous chapter for the purposes of the forward solution. The Debye parameters of the oil in the imaging region are assumed to be those given in Table 5.2, which gives a slightly less accurate match while allowing the oil to be modeled with the same relaxation time constants as the glycerol solutions. For the case of the 3-D printed phantom filled with glycerol solution, the plastic is assumed to be non-dispersive.

Initial and Termination Conditions

As in Chapter 3, the initial guess for the DBIM is chosen as the volumetric mean for the Debye parameters. The initial guess parameters for each imaging case are given in Table 5.3. The DBIM is terminated after four iterations. At this point, the change in residual is around a few percent of the residual for the initial guess. Running the DBIM past this point will likely lead to greater

Table 5.2: Debye parameters assumed for reconstructions

Phantom material	ε_∞ (or ε_r)	$\Delta\varepsilon$	σ_s (or σ_{eff}) (S/m)	τ_1 (ps)	τ_2 (ps)
3-D-printed ABS plastic	2.25	0	0.0035		
Triton X-100	4.5		0.11		
90%-10% glycerol-water solution	6.6	17.6	0	187	744
80%-20% glycerol-water solution	8.1	24.4	0	118	492
safflower oil (in V only)	2.6	0.3	0	118	492

Table 5.3: Initial guess for each reconstruction

Imaging case	ε_∞ (or ε_r)	$\Delta\varepsilon$	σ_s (or σ_{eff}) (S/m)
Plastic phantom with Triton X-100	2.9		0.033
Plastic phantom with 90% glycerol	3.5	5.1	0
25-mm test tube of 80% glycerol	3.1	2.7	0
13-mm test tube of 80% glycerol	2.8	1.0	0
Four 25-mm test tubes of 80% glycerol	3.2	6.3	0

error in the resulting image, as a great proportion of the residual vector is composed of model error contributions to the scattered signal.

5.4 Results and discussion

We first report the results from imaging the 3-D-printed plastic phantom filled with Triton X-100. For this case, the immersion medium of the array is air, instead of safflower oil. This moves the TM_{100} and TM_{300} frequency bands to 1.69 GHz and 3.16 GHz, respectively. We apply only the lower-band data to the reconstruction. Creating reconstructions of this type allow us to test the effect of the window on the imaging results for a relatively less-challenging imaging case, wherein the contrast between the constituent materials is small (which makes the Born approximation more

Table 5.4: Median γ between empty-array measurement and simulation for an air immersion (dB)

Window span (ns)	1.67 GHz	1.69 GHz	1.71 GHz
10	14.1	14.2	14.6
20	14.6	16.5	12.4
30	12.1	15.2	5.9
40	8.0	13.6	2.6

accurate), there is no ambiguity in immersion properties, and the more corrupted upper frequency band is excluded.

The bottom row of antennas on the lateral array panels do not have coverage of the phantom, and so are not used for the reconstruction. Likewise, the antennas on the bottom panel are also not used. This leaves the antennas in the top two rows, for a total of 20 active antennas. This same subset of antennas are active in all subsequent experimental imaging cases in this chapter.

We create reconstructions based on both the experimental data acquisition and a simulated data acquisition. Windows of 10, 20, 30, and 40 ns are used. For all cases, the boundaries of the imaging region V are coincident with the outer boundaries of the plastic phantom.

Table 5.4 reports the perturbation between measurement and simulation of the empty array using (4.4) for each of the frequencies used in the reconstruction and for each of the chosen window spans. The most even performance across the three frequencies are for the 10 ns and 20 ns windows. Increasing the length of the window increases the amount of model error between simulation and measurement. The increase in the degree of model error for longer windows may be due to compounding errors that occur with each reflection in the array. Alternatively, convolving with the sinc function may lead to signal components in adjacent frequency bins being summed coherently, while model error components in adjacent bins being summed non-coherently, effectively increasing the ratio between true signal and model error corruption.

Fig. 5.4 shows cross-sections through reconstructions of the plastic phantom filled with Triton X-100. Reconstructions from both the experimental and simulated data acquisition are shown using a variety of different window spans. The reconstructed dielectric constant is shown. As

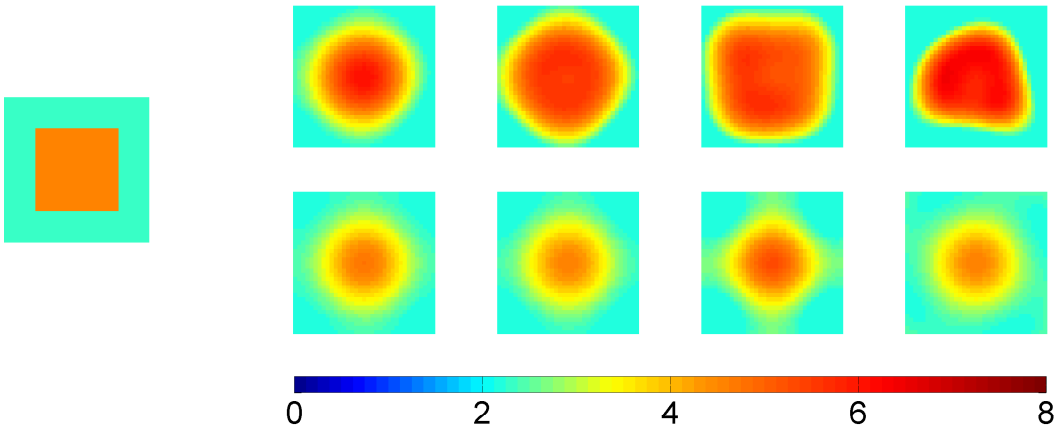

Figure 5.4: (a) A cross-section through the assumed exact profile for the 3-D-printed plastic phantom filled with Triton X-100. (b) Cross-sections through 3-D reconstructions of the phantom. Top row: reconstructions from experimental data. Bottom row: reconstructions from simulated data. The window spans used are (left to right) 10 ns, 20 ns, 30 ns, and 40 ns. Colorbar is ε_r.

described in the previous section, the reconstructed σ_{eff} is constrained to be highly correlated with the reconstructed ε_r, and is thus not shown. The simulated-data reconstructions commit the inverse crime, in which the data acquisition has no noise added to it and operates on the same grid as the forward solution, therefore avoiding any model error between the total and incident fields. Comparing experimental-data to simulated-data reconstructions is helpful in that it shows how much effect scattered signal corruption through noise, interference, or model error has on the experimental image. Each simulated-data reconstruction is very similar, suggesting that the span of the time-domain window applied to the data has little effect on the reconstruction for the case where there is no signal corruption. The experimental-data reconstructions are moderately over-estimated in comparison to the simulated-data reconstructions. The shape of the reconstructed regions in the simulated and experimental case are very similar for the 10 ns window. As the length of the window increases, progressively greater aberrance occurs in the shape of the experimentally-reconstructed regions. This result is consistent with the results in Table 5.4 and suggests that using a relatively

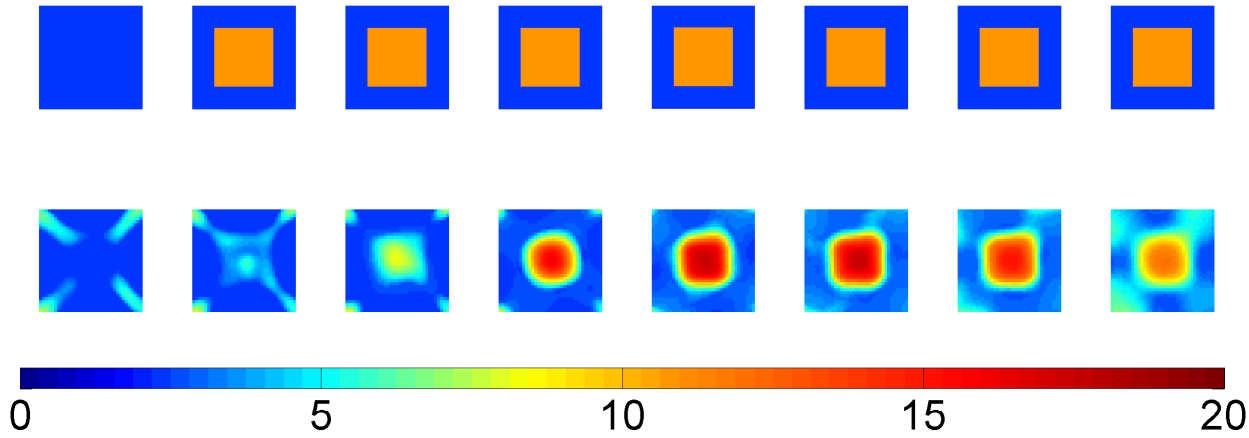

Figure 5.5: Top row: cross-sections through the assumed exact profile of the plastic phantom filled with an 90%-10% glycerol-water solution. Bottom row: cross-sections through the 3-D experimental Debye-parameter reconstruction. Both are shown in terms of ε_r at 1.6 GHz. Adjacent cross-sections are separated vertically by 1 cm.

short window is crucial in experimentally imaging with the enclosed array. The remainder of the reconstructions in this chapter will make use of a 10 ns window.

We next attempt a more challenging imaging scenario with the plastic phantom, in which the liquid in the phantom void is switched to the 90%-10% glycerol-water solution. The glycerol solution provides an 5:1 contrast in permittivity with the printed plastic. This is significantly greater than the 2:1 contrast between Triton X-100 and the printed plastic, and therefore makes the Born approximation less accurate. We also switch to a safflower oil immersion in order to match the eventual clinical imaging scenario. Lastly, we also introduce the experimental data from the upper frequency band.

Fig. 5.5 shows cross-sections through the experimental 3-D dielectric reconstruction of the plastic phantom filled with the glycerol solution. Debye parameters ε_∞ and $\Delta\varepsilon$ are reconstructed at each voxel. The resulting dielectric constant at 1.6 GHz is pictured. As in Fig. 5.4, the reconstructed dielectric parameters are constrained to be highly correlated, and so the reconstructed σ_{eff} is not shown. The reconstruction is visually very faithful to the exact dielectric profile. The higher

spatial frequencies of the scattered fields used for the reconstruction, which result from both the higher-permittivity immersion medium and the addition of the upper frequency band, cause the reconstructed liquid-filled void region to better approximate the square shape of the true phantom void cross-section. The vertical length of the liquid-filled void is also well-approximated. A small amount of aberrance is present in the reconstruction, most likely due to the more challenging scenario presented by the higher-contrast liquid in the void. These results demonstrate the ability of the experimental imaging system to successfully perform a high-contrast Debye-parameters reconstruction using multiple frequency bands and the desired immersion medium for eventual clinical imaging.

We next report the results of imaging test tubes of 80%-20% glycerol-water solution immersed in safflower oil. This imaging set allows us to demonstrate the robustness of the imaging system to high-contrast objects of various sizes and configurations. It also allows us to create reconstructions wherein both materials in the imaging region are dispersive. For this test set, the imaging region V is a square cylindrical region of dimensions 90 mm long by 70 mm wide, centered laterally in the array and descending downward from the hole in the top panel. Thus, V is of the same size and shape as the cylindrical phantom used in the imaging sets previously described.

We create images for four different test cases. The first is for the 13-mm-diameter tube centered laterally in the array. The second is for the 25-mm-diameter tube in the same position. These two cases allow us to show the effect of different sizes of target on the resulting image. The third case is for the 25-mm-diameter tube offset from center by 2 cm. The last case is for four 25-mm-diameter tubes arranged in a square formation. These final two cases allow us to show the effect of different target position and configuration on the resulting image.

Fig. 5.6 shows cross-sections through the experimental 3-D dielectric reconstructions of the various test tube configurations. In all four cases, there is substantial visual agreement between the reconstructions and the assumed exact profile. The reconstructed glycerol regions are accurately located, and their cross-sectional areas are very similar to the true cross-sectional area of the test objects. The reconstructed glycerol region for the 13-mm tube is significantly underestimated, which is to be expected, given its small cross-sectional area. The reconstructions of the

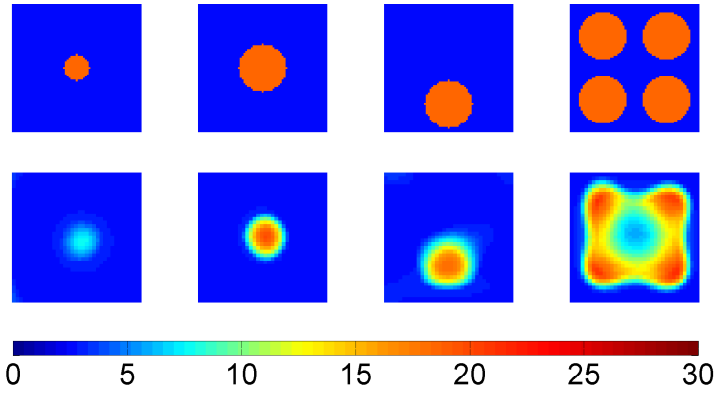

Figure 5.6: Top row: cross-sections through the assumed exact profile of several imaging cases using various configurations of test tubes filled with an 80%-20% glycerol-water solution. Bottom row: cross-sections through the resulting 3-D experimental Debye-parameter reconstructions. Both are shown in terms of ε_r at 1.6 GHz.

single 25-mm tube achieve permittivities that are very close to the measured properties of 80% glycerol. For the case of the four 25-mm tubes, each tube is identifiable in the image, although the high-permittivity parts of the reconstruction bleed into one another to some extent. These results demonstrate the ability of the imaging algorithm to reconstruct dielectric profiles for high-contrast targets of varying size and position, as well as its ability to discriminate between multiple targets in the imaging region.

5.5 Conclusion

In this chapter, we acquired experimental data from a series of simple objects using the enclosed array of miniaturized, multi-band patch antennas described previously. We described the modifications to the imaging algorithm that were made for experimental reconstruction, including row and column weighting and windowing. The dielectric reconstruction results for each test object were reported. Applying a relatively short (10 ns) window to the signals from measurement

and forward solution led to a decreased overall degree of model error and therefore scattered signal corruption, which resulted in more accurate reconstructions. A 3-D-printed square cylindrical phantom filled with different liquids for contrast was successfully imaged, as were test tubes of glycerol solution with different sizes and configuration. The basic shape and position for all target objects were accurately reconstructed.

Chapter 6

Construction and Experimental Imaging of an MRI-derived 3-D-printed Breast Phantom

6.1 Introduction

Image validation is crucial for both development and performance evaluation of microwave breast imaging strategies. It involves comparing the estimated dielectric profile with the profile of the imaging testbed in order to ascertain accuracy in both the reconstructed dielectric properties and the reconstructed interior structure. Clinical imaging with human subjects [50, 52] provides the most faithful test domain; however, validation of clinical microwave images is challenging, as the true in vivo dielectric distribution is unknown. Alternatively, numerical studies using MRI-derived numerical phantoms [57, 63], are a powerful tool for evaluating imaging strategies, as the reconstructed dielectric profiles can be compared directly and unambiguously to the true testbed, which is realistic in both dielectric properties and interior structure. Numerical studies do not, however, introduce the complications inherent in experimental imaging, such as imperfect antenna modeling and environmental interference. Anthropomorphic, heterogeneous experimental breast phantoms will therefore play a critical role in pre-clinical imaging studies.

Several previous studies have reported experimental phantoms that have anthropomorphic exterior surfaces and are constituted by synthetic materials that approximate (to varying degrees of

Sections 6.1 and 6.2 are partially adapted from M. Burfeindt, T. Colgan, R. Mays, J. Shea, N. Behdad, B. Van Veen, and S. Hagness. "MRI-derived 3-D-printed Breast Phantom for Microwave Breast Imaging Validation," *IEEE Antennas and Wireless Propagation Letters*, vol. 11, pp. 1610 - 1623. [77]. The work in the remaining sections was performed in collaboration with the same co-authors.

accuracy) the dielectric properties of skin, fibroglandular, and adipose tissue. These phantoms have interiors that are either homogeneous (e.g., adipose-tissue simulant enclosed by a thin layer of skin simulant) [72], homogeneous except for a target inclusion (e.g., malignant-tissue simulant) [79,80], or heterogeneous [49,81,82]. Heterogeneity is achieved by distributing fibroglandular tissue simulants non-uniformly in the phantom interior. In the examples of [81,82], a high degree of dielectric properties realism is achieved through the use of tissue-mimicking oil-in-gelatin dispersions [83]. However, it is difficult to use the phantom construction methods of [81]- [82] to distribute fibroglandular tissue simulants throughout the adipose-tissue simulant in such a way as to realistically mimic the structural complexity of the interior of the breast. Experimental phantoms that provide a more accurate representation of the interior breast structure, even if at the expense of dielectric properties accuracy, will play an important complementary role in validating the ability of microwave imaging strategies to resolve realistic structural features of breast tissue.

Recent advances in three-dimensional (3-D) rapid prototyping technology allow the printing of highly complex plastic objects from precise computer models. In this chapter, we describe an MRI-derived 3-D-printed breast phantom for experimental validation of microwave breast imaging. The portion of the model that is printed in plastic corresponds to locations of adipose tissue, while the void in the model corresponds to locations of fibroglandular tissue. Both the exterior and interior of the model are derived from an MRI of a human subject. Thus the exterior is anthropomorphic while the interior spatial layout of the void within the plastic is correlated strongly with a realistic distribution of fibroglandular tissue surrounded by adipose tissue. The 3-D-printed phantom is thus a promising test object for validating microwave inverse scattering techniques and systems designed for microwave breast imaging.

In the following sections, we first describe the procedure for constructing the 3-D-printed breast phantom. We then fill the phantom void with a liquid that provides a biologically-relevant dielectric contrast with the plastic – one that mimics the contrast between fibroglandular and adipose tissue. An experimental data acquisition for the phantom is then performed using the enclosed array of miniaturized patch antennas. The experimental imaging algorithm described in the last chapter is then applied to the data, and the resulting images are compared to the phantom model. The

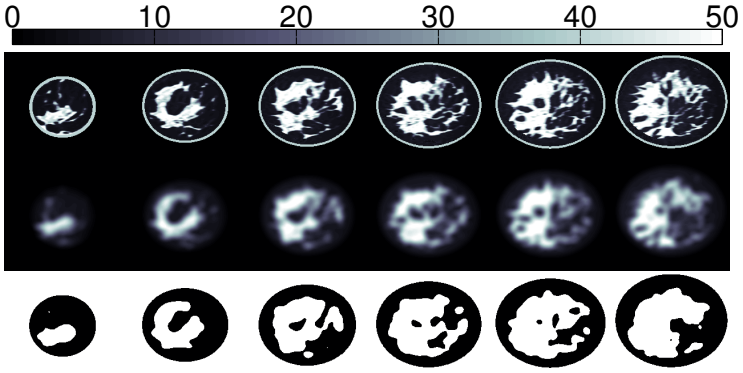

Figure 6.1: Cross-sections through (top row) the 3-D profile of ε_s for a Class 3 (heterogeneously dense) numerical breast phantom, (middle row) the blurred 3-D distribution, and (bottom row) the thresholded 3-D binary model. For the binary model, black corresponds to the portion to be printed in plastic and white corresponds to the void. Adjacent cross-sections are separated by 1 cm.

reconstructed dielectric profile is shown to be very visually similar to the exact phantom profile, which demonstrates the ability of the array and algorithm for imaging targets with biologically-relevant contrast and complexity.

6.2 Phantom construction

The 3-D-printed breast phantom was derived from a heterogeneously dense (Class 3 in terms of BI-RADS density) numerical breast phantom in the University of Wisconsin Computational Laboratory (UWCEM) breast phantom repository [1]. The numerical phantom is MRI-derived, and is thus anthropomorphic and heterogeneous with realistic interior tissue structure. Coronal cross-sections through the dielectric profile of the numerical phantom are shown in Fig. 6.1 (top row).

Constructing the printed phantom model involves creating a volumetric binary mask that differentiates between solid plastic and air void regions. This requires removing the numerical phantom's skin layer and segmenting the fibroglandular regions from the adipose regions. However,

simply thresholding the numerical phantom to identify regions of fibroglandular tissue may lead to the erroneous creation of non-contiguous solid regions that fall out of the phantom, and/or non-contiguous isolated voids that cannot be filled with liquid.

We avoided this problem by convolving the distribution of Debye parameter ε_s (static permittivity) with a spherical Gaussian blurring function of variance 25 mm^2 and support radius of 4.5 mm. Fig. 6.1 (middle row) shows cross-sections through the blurred dielectric distribution. We then thresholded the blurred numerical phantom at $\varepsilon_s = 15$. Voxels below the threshold (that is, voxels nearest to adipose tissue in dielectric properties) were designated as belonging to the solid part of the model, while voxels above the threshold (that is, voxels nearest to fibroglandular tissues in dielectric properties) were designated as belonging to the void. Cross sections through the resulting binary phantom model are shown in Fig. 6.1 (bottom row). The binary model is very heterogeneous; the void regions preserve the location and shape of fibroglandular tissue structures in the original phantom, albeit with a slightly reduced spatial resolution. All void regions are contiguous, allowing them to be filled with a single liquid solution.

A slab of dimensions $170 \times 170 \times 5$ mm was added to the posterior base of the model. The slab enables positioning the printed breast phantom in the enclosed array of miniaturized, multi-band patch antennas.

3-D printers typically require computer models in the form of a series of 2-D facets that describe the surfaces composing the object to be printed. We used the volumetric binary breast model (e.g., bottom of Fig. 6.1) to generate a series of surface facets representing both the outer surface of the phantom and the surface of the interior void. The facet model was then exported to a Dimension Elite 3-D Printer (Dimension, Inc., Eden Prairie, MN), which printed the phantom using acrylonitrile butadiene styrene (ABS) plastic. The nominal spatial resolution of the 3-D printer is between 0.178 mm and 0.254 mm, which is at least two orders of magnitude smaller than the wavelength in the UHF band. The printing process took approximately 36 hours. Photographs of the resulting 3-D-printed breast phantom prior to filling the air voids with liquid are shown in Fig. 6.2.

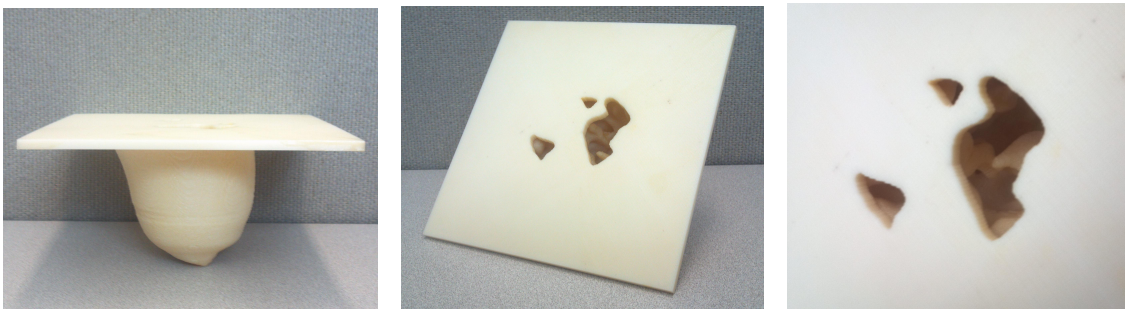

(a) **(b)** **(c)**

Figure 6.2: Photographs of the 3-D-printed breast phantom (prior to filling the fibroglandular void regions with liquid). (a) Side view shows the anthropomorphic exterior of the phantom with a support slab on top. (b)-(c) Top views show the openings in the top slab which reveal the heterogeneous interior (voids in regions corresponding to fibroglandular tissue, and plastic in regions corresponding to adipose tissue).

To create a contrast between the phantom void and the 3-D-printed plastic, we fill the void with a solution of 90% glycerol and 10% deionized water. The measured dielectric properties of this solution are given in Table 5.1. The magnitude of the ratio of intrinsic impedance between the glycerol solution and the printed plastic is about 0.4 at 2 GHz. This is comparable to the magnitude of the ratio of intrinsic impedance between 25th percentile fibroglandular tissue and 75th percentile adipose tissue at 2 GHz, which is 0.45 using the Cole-Cole models reported in [1].

6.3 Imaging results and discussion

We acquired experimental microwave data from the MRI-derived phantom filled with 90% glycerol using the enclosed array of miniaturized antennas from previous chapters. The immersion medium was safflower oil. We applied the experimental data to the DBIM imaging algorithm as described in Chapter 5 in order to create a Debye parameter recontruction in terms of ε_∞ and $\Delta\varepsilon$. The 20 antennas in the top two rows of the array are active. A 10 ns rectangular time-domain window was applied to all forward solution electric fields, and the corresponding frequency-domain sinc function window was convolved with the experimental data acquisition data. Frequencies

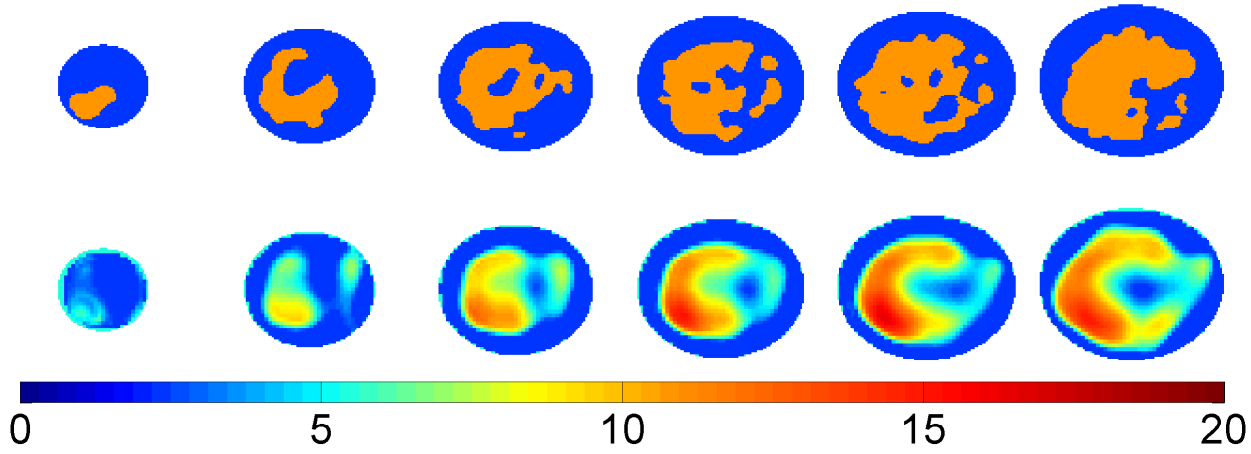

Figure 6.3: Coronal cross-sections through (top row) the printed phantom model and (bottom row) the 3-D Debye parameter reconstruction based on an experimental data acquisition. Both are shown in terms of ε_r at 1.6 GHz. Adjacent cross-sections are vertically separated by 1 cm.

from the TM_{300} band were penalized by a factor of five using row weighting. The two Debye parameters at each voxel in the reconstruction domain were constrained to be highly correlated via the projected restart algorithm. The imaging region V was chosen to comprise all interior points of the phantom. This required *a priori* knowledge of the phantom's outer surface.

Fig. 6.3 shows cross-sections through the 3-D reconstruction resulting from applying the imaging algorithm to the experimental data acquisition. Blue regions correspond to plastic regions, while orange corresponds to the fluid-filled void. Visual fidelity between the reconstruction and the phantom model is evident in all cross-sections. The glycerol regions are reconstructed accurately in terms of their basic shape and location. Resolution is moderate, but smaller details of some features can still be identified. These results demonstrate that the algorithm applied to experimental data acquisition from the enclosed array of miniaturized, multi-band patch antennas can effectively image target distributions of biologically-relevant complexity.

Higher resolution images may be accomplished by making modifications to the antennas in the array. The TM_{300} band at 3.06 GHz is high enough to achieve sufficient resolution. However, this band is significantly more corrupt due to model error, as was reported in Chapter 4. The degree

of model error may in general increase with higher frequencies. Thus, using a miniaturized patch antenna with a lower TM_{300} band may lead to a lesser degree of model error, which would necessitate less severe frequency penalties and allow higher spatial frequencies into the reconstruction. Previous work using simulated data acquisition from an array of ideal dipole antennas has accomplished higher resolution using a maximum frequency of 2.5 GHz [57]. Moving the higher band of the patch antenna to a lower frequency may be accomplished through the addition of more slots on the patch surface [68,84]. This would likely result in a loss of gain in the antenna; however, this tradeoff would be beneficial, as the increased degree of noise corruption due to the lower antenna gain would likely still be several orders of magnitude below the degree of model error corruption of the scattered signal.

6.4 Conclusion

We proposed an MRI-derived, 3-D-printed breast phantom for use in microwave breast imaging experiments. The interior structure of the phantom is very similar to a realistic distribution of fibroglandular and adipose tissue. Microwave images can be compared directly to the 3-D binary model used for printing the phantom, permitting unambiguous co-registration between the phantom interior structure and the reconstructed dielectric profile. The void of the 3-D-printed model was filled with a dispersive liquid in order to provide a biologically-relevant dielectric contrast with the printed plastic. We acquired experimental data from the phantom using an enclosed array of miniaturized patch antennas and reconstructed the phantom dielectric profile using the DBIM. The resulting image was very similar to the exact dielectric profile of the phantom, demonstrating the effectiveness of the imaging system to experimentally reconstruct target distributions with biologically relevant complexity. A higher degree of anatomical realism may be achieved in future studies by coating the outside of the phantom with a skin-mimicking material, while a small object may be suspended in the liquid to approximate the presence of a tumor in fibroglandular tissue.

Chapter 7

Beamforming-Enhanced Inverse Scattering for Microwave Breast Imaging

7.1 Introduction

For a given data acquisition system, a degree of signal corruption is unavoidable. The sensitivity of the microwave imaging algorithm to signal corruption may be improved through the incorporation of focal transmit-receive beamforming techniques into the data acquisition process. In the context of antenna arrays, transmit beamforming involves modifying the magnitude and phase of the signal fed to each antenna in such a way as to achieve constructive interference, and thus stronger transmitted signal, in a desired propagation direction. Likewise, receive beamforming is accomplished by modifying the magnitude and phase of the received signal in order to emphasize reception from a desired direction. Modifying the magnitude and phase of the outgoing or incoming signal is accomplished by multiplying the complex signal phasor in each channel by a complex beamforming weight. Beamforming can lead to an increase to the effective signal-to-noise ratio (SNR), as signal from targets in the desired propagation direction is summed coherently, whereas noise is assumed to be non-correlated and is thus summed non-coherently. Non-focal beamforming for the inverse scattering problem has been reported by Abubakar et al [85] for the purpose of decreasing the computational cost of the inverse solution. This work used the singular vectors

This chapter is partially adapted from M. Burfeindt, B. Van Veen, and S. Hagness. "Beamforming-Enhanced Inverse Scattering for Microwave Breast Imaging," *USNC-URSI National Radio Science Meeting*, Boulder, CO, Jan. 2012.

of the matrix of scattered fields from the antenna array as beamforming weights. By discarding scattered field data corresponding to the smallest singular values, the size of the linear system to be solved was decreased. Discarding enough data also led to an improvement in the performance of the algorithm when applied to noisy data. The boost in noise performance was observed for simulated data experiments that used a very large number of antennas (160), perhaps leading to a large amount of redundant scattered field data that could safely be discarded.

In this study, we formulate a focal beamforming-enhanced version of the distorted-Born iterative method (DBIM) with the goal of decreasing the noise sensitivity of the imaging algorithm. This approach involves designing beamforming weights for a series of foci in the imaging volume such that the SNR for the signal from each focus is maximized. In this way, improvements in noise performance can be achieved without discarding valuable scattered field data. In this study, we apply both the beamforming-enhanced and standard DBIM algorithms to simulated electric field data to create 3-D reconstructions of the dielectric profiles of two MRI-derived, anatomically realistic numerical breast phantoms. We evaluate the performance of the beamforming-enhanced DBIM algorithm relative to the standard algorithm for a wide range of SNR and show that the beamforming-enhanced reconstructions are significantly more faithful to the true dielectric profiles than are the standard reconstructions for SNR below 15 dB. These results demonstrate the advantages of focal beamforming when signal corruption is significant and suggest that further study is warranted.

7.2 Numerical domains for data acquisition simulations

The heterogeneous, anthropomorphic numerical breast phantoms used in this study are derived from MR scans of human subjects as described in detail in [1]. The range of dielectric properties for each tissue type is defined according to the large-scale study conducted by Lazebnik et al. [32]. As in [57], the dispersive dielectric properties at each voxel in the breast volume are modeled using a single-pole Debye model with relaxation constant $\tau = 15$ ps.

Simulated electric field data was acquired from the Class 2 (scattered fibroglandular) and Class 3 (heterogeneously dense) breast phantoms. The phantoms were surrounded by a 40-element array

of 14-mm dipoles, in the same manner as in [57]. The dipoles were distributed across five elliptical rings of eight elements each. The major and minor axes of each ring were scaled so that there is a minimum 1-mm spacing between each element and the breast surface. Adjacent rings were rotated by 22.5°. The phantoms and the arrays are immersed in a lossless, non-dispersive coupling medium with dielectric constant of 2.6.

Data acquisition was performed via FDTD on a 0.5-mm uniform grid. Transmitting antennas were gap-fed with a vertical (z-oriented) current source density. Received electric field data were collected at 1, 1.5, 2, and 2.5 GHz and converted to phasor form via discrete Fourier transform (DFT).

7.3 Transmit-receive beamforming-enhanced DBIM

We assume an imaging setup of the same form as is given in Sec. 2.3. Using the Born approximation and the scalar approximation, we can simplify (2.2) to

$$E^s(\mathbf{r}_{\rm src}, \mathbf{r}_{\rm rec}) = E^t(\mathbf{r}_{\rm src}, \mathbf{r}_{\rm rec}) - E^i(\mathbf{r}_{\rm src}, \mathbf{r}_{\rm rec}) = \omega^2 \mu_0 \varepsilon_0 \int_V G^b(\mathbf{r}', \mathbf{r}_{\rm rec}) E^i(\mathbf{r}_{\rm src}, \mathbf{r}') o(\mathbf{r}') d^3\mathbf{r}' \quad (7.1)$$

The latter simplification assumes that the co-polarized electric field component dominates the cross-polarized components in the reconstruction region V. Using the relation

$$E^i = -j\omega\mu_0\varepsilon_0 \ell_s i(\omega) G^b(\mathbf{r}', \mathbf{r}_{\rm rec}), \quad (7.2)$$

where $i(\omega)$ is the source current and ℓ_s is the source length, (7.1) can be written

$$E^s(\mathbf{r}_{\rm src}, \mathbf{r}_{\rm rec}) = -j\omega^3 \mu_0^2 \varepsilon_0 \ell_s i(\omega) \int_V G^b(\mathbf{r}_{\rm rec}, \mathbf{r}') G^b(\mathbf{r}_{\rm src}, \mathbf{r}') o(\mathbf{r}') d^3\mathbf{r}'. \quad (7.3)$$

Eq. (7.2) differs from (3.1) in that it is written in terms of a source current, as opposed to a resistive voltage source. Eq. (7.3) forms the basis for standard DBIM.

Transmit-receive Beamforming

Each antenna has associated with it a complex channel transmit weight that modifies the phase and amplitude of $i(\omega)$ before transmission. The weights are designed at a specific frequency, ω, to

achieve a focus at location $\mathbf{r}'_{\rm f}$. The channel transfer weights are represented in vector form as

$$\mathbf{w}_t(\mathbf{r}'_{\rm f},\omega) = [w_{t1}(\mathbf{r}'_{\rm f},\omega)w_{t2}(\mathbf{r}'_{\rm f},\omega)\ldots w_{tL}(\mathbf{r}'_{\rm f},\omega)]^{\rm H} \tag{7.4}$$

where $w_{ti}(\mathbf{r}'_{\rm f},\omega)$ represents the complex channel weight for the ith antenna and 'H' denotes the conjugate transpose. Let the Green's function vector be

$$\mathbf{g}_b(\mathbf{r}',\omega) = \left[G^b(\mathbf{r}_1,\mathbf{r}')G^b(\mathbf{r}_2,\mathbf{r}')\ldots G^b(\mathbf{r}_L,\mathbf{r}')\right]^{\rm T}, \tag{7.5}$$

where $\mathbf{r}_1\ldots\mathbf{r}_L$ are the locations of the L antennas. Let the incident field at $\mathbf{r}'_{\rm f}$ due to transmit beamforming with weight vector $\mathbf{w}_t(\mathbf{r}'_{\rm f},\omega)$ be denoted $\tilde{E}^i(\mathbf{r}',\mathbf{r}'_{\rm f})$, given by

$$\tilde{E}^i(\mathbf{r}',\mathbf{r}'_{\rm f}) = -j\omega\mu_0\varepsilon_0\ell_s i(\omega)\mathbf{w}_t^{\rm H}(\mathbf{r}'_{\rm f},\omega)\mathbf{g}_b(\mathbf{r}',\omega). \tag{7.6}$$

Let $\tilde{E}^s(\mathbf{r}_{\rm rec})$ be the scattered field seen at $\mathbf{r}_{\rm rec}$ due to transmit beamforming with weight vector $\mathbf{w}_t(\mathbf{r}'_{\rm f},\omega)$. From (7.1) and (7.6), we obtain the relation

$$\tilde{E}^s(\mathbf{r}_{\rm rec}) = -j\omega^3\mu_0^2\varepsilon_0\ell_s i(\omega)\int_V G^b(\mathbf{r}_{\rm src},\mathbf{r}')\mathbf{w}_t^{\rm H}(\mathbf{r}'_{\rm f},\omega)\mathbf{g}_b(\mathbf{r}',\omega)o(\mathbf{r}')d^3\mathbf{r}'. \tag{7.7}$$

Each antenna has associated with it a complex channel receive weight that modifies the phase and amplitude of the received signal resulting from the scattered field in (7.7). The channel weights are designed to receive electric fields from focus location $\mathbf{r}'_{\rm f}$. Let the receive channel weight vector be denoted $\mathbf{w}_r(\mathbf{r}'_{\rm f},\omega)$. The modified received signals are summed to form the beamformer output signal $s(\mathbf{r}'_{\rm f},\omega)$, given by

$$\begin{aligned} s(\mathbf{r}'_{\rm f},\omega) &= -j\omega^3\mu_0^2\varepsilon_0\ell_s i(\omega)\int_V \mathbf{w}_r^{\rm H}(\mathbf{r}'_{\rm f},\omega)\mathbf{g}_b(\mathbf{r}',\omega)\mathbf{w}_t^{\rm H}(\mathbf{r}'_{\rm f},\omega)\mathbf{g}_b(\mathbf{r}',\omega)o(\mathbf{r}')d^3\mathbf{r}' \\ &= \mathbf{w}_t^{\rm H}(\mathbf{r}'_{\rm f},\omega)\mathbf{D}(\omega)\mathbf{w}_r^*(\mathbf{r}'_{\rm f},\omega), \end{aligned} \tag{7.8}$$

where '*' denotes the complex conjugate and $\mathbf{D}(\omega)$ is the $L\times L$ bistatic scattering matrix given by $D_{mn} = E_s(\mathbf{r}_{\rm rec},\mathbf{r}_{\rm src})$. Eq. (7.8) shows that transmit-receive beamforming can be accomplished by acquiring $\mathbf{D}$, designing the weights $\mathbf{w}_t$ and $\mathbf{w}_r$, and multiplying. Returns from multiple foci can be obtained in post-processing by designing $\mathbf{w}_t$ and $\mathbf{w}_r$ for each focus. Thus, it is not necessary to design and implement beamforming hardware such as delay lines for measurement from each focus location.

It is generally desired to exclude monostatic data, wherein the same antenna acts as transmitter and receiver, from the microwave inversion [57]. Monostatic data may be removed from (7.8) by replacing the diagonal components of $\mathbf{D}$ with zeros and subtracting the term

$$\zeta(\mathbf{r}'_{\mathrm{f}}, \mathbf{r}') = \left(\mathbf{w}_t(\mathbf{r}'_{\mathrm{f}}, \omega) \odot \mathbf{w}_r(\mathbf{r}'_{\mathrm{f}}, \omega)\right)^{\mathrm{H}} \left(\mathbf{g}_b(\mathbf{r}', \omega) \odot \mathbf{g}_b(\mathbf{r}', \omega)\right) \tag{7.9}$$

from the integrand, where $\odot$ is pointwise vector multiplication.

In general, $\mathbf{w}_t$ and $\mathbf{w}_r$ may be different. For this study, we choose for the transmit and receive weights to be identical. For a focus location $\mathbf{r}'_{\mathrm{f}}$, the weights are chosen to satisfy the maximum SNR criterion [19], given by

$$\mathbf{w}(\mathbf{r}'_{\mathrm{f}}, \omega) = \arg \max_{\mathbf{w}(\mathbf{r}'_{\mathrm{f}}, \omega)} \frac{\mathbf{w}^{\mathrm{H}}(\mathbf{r}'_{\mathrm{f}}, \omega)\mathbf{g}_b(\mathbf{r}'_{\mathrm{f}}, \omega)\mathbf{g}_b^{\mathrm{H}}(\mathbf{r}'_{\mathrm{f}}, \omega)\mathbf{w}(\mathbf{r}'_{\mathrm{f}}, \omega)}{\mathbf{w}^{\mathrm{H}}(\mathbf{r}'_{\mathrm{f}}, \omega)\mathbf{\Sigma}\mathbf{w}(\mathbf{r}'_{\mathrm{f}}, \omega)}, \tag{7.10}$$

where $\mathbf{\Sigma}$ is the noise covariance matrix. The solution to (7.10) is $\mathbf{w}(\mathbf{r}'_{\mathrm{f}}, \omega) = \alpha\mathbf{\Sigma}^{-1}\mathbf{g}_b(\mathbf{r}'_{\mathrm{f}}, \omega)$, where α is an arbitrary constant. For Gaussian white noise, $\mathbf{\Sigma}$ is the identity matrix. We choose $\alpha = 1/||\mathbf{g}_b(\mathbf{r}'_{\mathrm{f}}, \omega)||_2$ for this study.

The Imaging Algorithm

The goal of both the standard DBIM algorithm and the beamforming-enhanced DBIM algorithm is to reconstruct the unknown dielectric profile in the imaging region V. The standard DBIM operates on (7.3), while the beamforming-enhanced DBIM operates on (7.8).

The forward solution is performed via FDTD on a uniform 2-mm grid. The incident electric fields are recorded at all antenna feed locations and at all voxels in V. Incident fields are converted to Green's functions via (7.2). They are then converted to phasor form via DFT.

The difference in grid resolution between the data acquisition and forward solution simulations leads to model mismatch which can introduce error in the recorded scattered fields. We counteract this mismatch using a calibration procedure wherein we simulate an empty antenna array on both the 0.5- and 2-mm grids. For each transmit-receive channel, we compute a complex multiplicative calibration constant by dividing the electric field in the fine grid by the electric field in the coarse grid. The electric field phasors from the breast phantom data acquisition simulation

are then calibrated by dividing them on a channel-by-channel basis by the empty-array calibration constants.

Following calculation of the relevant field phasors, the $L \times L$ bi-static scattering matrix $\mathbf{D}(\omega)$ is formed for each frequency of interest. Also formed are the background Green's function vectors for each voxel in V, given by $\mathbf{g}_b(\mathbf{r}'_k, \omega)$, where $\mathbf{r}'_k$ is the location of the kth voxel in V.

For the mth focus location both the transmit and receive weights are chosen according to (7.10) to achieve $\mathbf{w}(\mathbf{r}'_{\mathrm{fm}}, \omega) = \mathbf{g}_{b0}(\mathbf{r}'_{\mathrm{fm}}, \omega)/||\mathbf{g}_{b0}(\mathbf{r}'_{\mathrm{fm}}, \omega)||_2$, where $\mathbf{g}_{b0}(\mathbf{r}'_{\mathrm{fm}}, \omega)$ is the background Green's function of the dielectric profile of the initial guess, i.e., the first DBIM iteration. The beamformer weights could be updated at each iteration to reflect the new background permittivity, but this approach is not used here. Foci are placed on a uniform grid in V, with a spacing given by Δ_{f} .

The vectors and matrices described above are used to form the inverse system $\mathbf{b} = \mathbf{A}\mathbf{x}$ used to solve for the unknown contrast. The unknown contrast vector $\mathbf{x}$ is given by (2.3). The single-frequency residual vector $\mathbf{b}$ is given by

$$\mathbf{b} = \begin{bmatrix} \Re\left\{\mathbf{w}_t^{\mathrm{H}}(\mathbf{r}'_{\mathrm{f}1}, \omega)\mathbf{D}(\omega)\mathbf{w}_r^*(\mathbf{r}'_{\mathrm{f}1}, \omega)\right\} \\ \vdots \\ \Re\left\{\mathbf{w}_t^{\mathrm{H}}(\mathbf{r}'_{\mathrm{f}M}, \omega)\mathbf{D}(\omega)\mathbf{w}_r^*(\mathbf{r}'_{\mathrm{f}M}, \omega)\right\} \\ \Im\left\{\mathbf{w}_t^{\mathrm{H}}(\mathbf{r}'_{\mathrm{f}1}, \omega)\mathbf{D}(\omega)\mathbf{w}_r^*(\mathbf{r}'_{\mathrm{f}1}, \omega)\right\} \\ \vdots \\ \Im\left\{\mathbf{w}_t^{\mathrm{H}}(\mathbf{r}'_{\mathrm{f}M}, \omega)\mathbf{D}(\omega)\mathbf{w}_r^*(\mathbf{r}'_{\mathrm{f}M}, \omega)\right\}, \end{bmatrix} \tag{7.11}$$

where the monostatic data has been removed from $\mathbf{D}$. The submatrix $\mathbf{A}^0$ is formed via discretization of (7.8) and is given by

$$A^0_{mk} = -j\Delta^3\omega^3\mu_0^2\varepsilon_0\ell_s i(\omega)\left\{\mathbf{w}_t^{\mathrm{H}}(\mathbf{r}'_{\mathrm{f}m}, \omega)\mathbf{g}_b(\mathbf{r}'_k, \omega)\mathbf{g}_b^{\mathrm{T}}(\mathbf{r}'_k, \omega)\mathbf{w}_r^*(\mathbf{r}'_{\mathrm{f}m}, \omega) - \zeta(\mathbf{r}_{\mathrm{f}m}, \mathbf{r}'_k)\right\}. \tag{7.12}$$

The matrix $\mathbf{A}$ is formed from $\mathbf{A}^0$ via (2.6). As in Chapter 2, the multiple-frequency inverse system is formed by creating $\mathbf{b}$ and $\mathbf{A}$ for each frequency and vertically concatenating.

The beamforming-enhanced DBIM algorithm reduces to the standard DBIM algorithm as described in Chapters 2 and 3 when the weights used are the standard real basis functions. Let the jth standard basis function be denoted $\mathbf{e}_j = [e_1\ e_2 \ldots e_L]^{\mathrm{T}}$, where $e_{h=j} = 1$, $e_{h\neq j} = 0$. For a

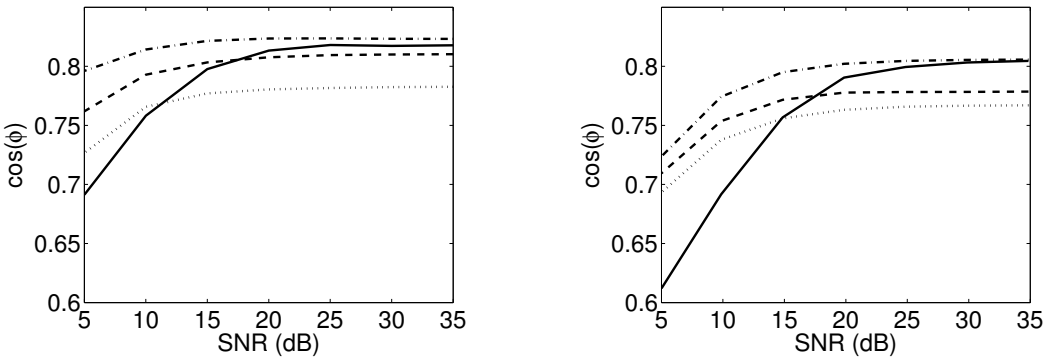

Figure 7.1: Quality metric $\cos(\phi)$ versus SNR for (a) the Class 2 and (b) Class 3 breast phantoms. Solid line: Standard DBIM. Dash-dot line: Beamforming-enhanced DBIM, $\Delta_{\mathrm{f}} = 1$ cm. Dash-dash line: Beamforming-enhanced DBIM, $\Delta_{\mathrm{f}} = 2$ cm. Dot-dot line: Beamforming-enhanced DBIM, $\Delta_{\mathrm{f}} = 3$ cm

channel formed by transmitting at the nth source and receiving at the mth source, $\mathbf{w}_r = \mathbf{e}_n$, while $\mathbf{w}_t = \mathbf{e}_m$. In this case, M is the number of channels instead of the number of foci. If all bistatic channels are used, excluding those formed by reciprocal antenna pairs, then $M = (L)(L-1)/2$.

The inverse solution is performed via CGLS. Regularization is achieved by terminating CGLS early via the L-curve method [86]. As in Chapter 3, the projected restart algorithm is used to constrain the three Debye parameters to be roughly proportional at each voxel.

The DBIM algorithm is considered to have converged in this study based on the convergence of the norm of the residual vector, $\mathbf{b}$. Let $\mathbf{b}^{(i)}$ be defined as the residual vector $\mathbf{b}$ at the ith DBIM iteration. Termination of the DBIM algorithm occurs when one of three conditions have been reached: 1) When ten DBIM iterations are performed; 2) when $||\mathbf{b}^{(i)}||_2 - ||\mathbf{b}^{(i-1)}||_2 < 0.01||\mathbf{b}^{(1)}||_2$; or 3) when $||\mathbf{b}^{(i)}||_2 > ||\mathbf{b}^{(i-1)}||_2 > ||\mathbf{b}^{(i-2)}||_2$. In the latter case, performing further iterations is unlikely to improve the quality of the reconstruction.

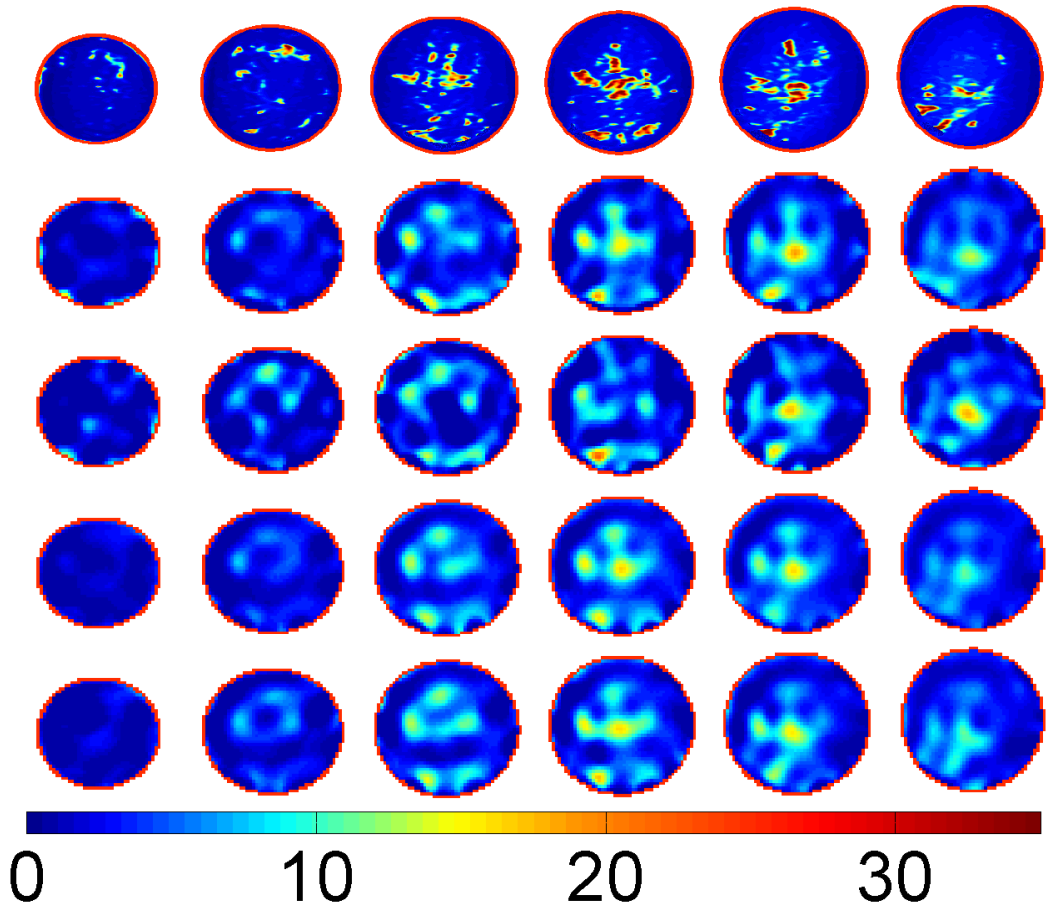

Figure 7.2: Top row: Exact dielectric profile of the Class 2 (scattered fibroglandular) phantom in terms of $\Delta\varepsilon$. Second and third rows: Standard DBIM reconstruction at 30 dB and 10 dB SNR, respectively. Fourth and fifth rows: Beamforming-enhanced reconstruction with $\Delta_{\mathrm{f}} = 1$ cm at 30 dB SNR and 10 dB SNR, respectively. Adjacent cross-sections are separated vertically by 1 cm.

7.4 Results and discussion

In this section we report the results from applying both the standard DBIM algorithm and the beamforming-enhanced DBIM algorithm to the synthetic data acquired from the numerical testbeds as described in Sec. 7.2. We report the results by displaying quantitative images of the Debye parameter reconstructions and by using the numerical quality metric $\cos(\phi)$ introduced in Chapter 3.

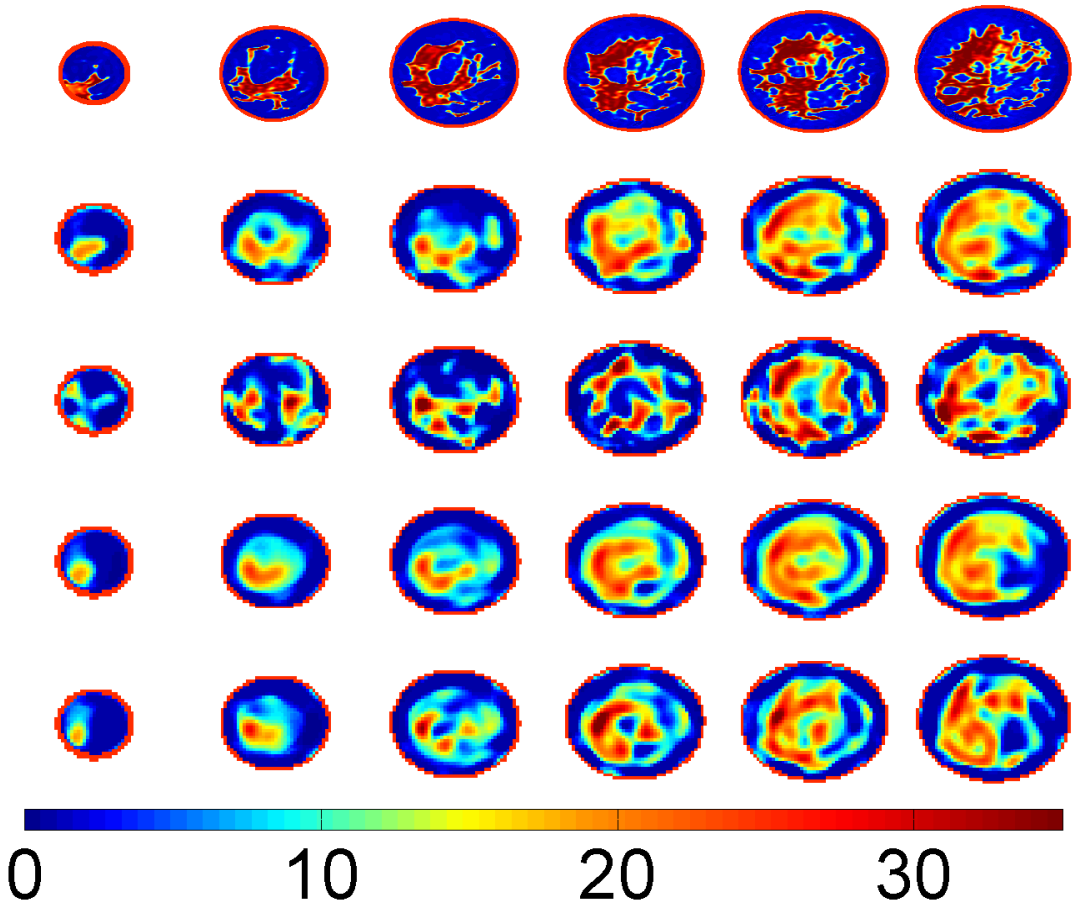

Figure 7.3: Top row: Exact dielectric profile of the Class 3 (heterogeneously dense) phantom in terms of $\Delta\varepsilon$. Second and third rows: Standard DBIM reconstruction at 30 dB and 10 dB SNR, respectively. Fourth and fifth rows: Beamforming-enhanced reconstruction with $\Delta_{\mathrm{f}} = 1$ cm at 30 dB SNR and 10 dB SNR, respectively. Adjacent cross-sections are separated vertically by 1 cm.

For each phantom class, reconstructions were created after Gaussian white noise was added to the data acquisition measurements. The SNR (referenced to received power) was varied from 35 dB to 5 dB in decrements of 5 dB. SNR is defined here as the ratio of the total received power across all channels to the total noise power across all channels. Four independent noise instances were generated for both phantom classes. At each designated SNR level, each noise instance was scaled appropriately and reconstructions were performed. The beamforming-enhanced reconstructions

were performed for Δ_{f} = 1, 2, and 3 cm. Thus, four standard reconstructions and 12 beamforming-enhanced reconstructions were performed for each SNR level.

Fig. 7.1 is a plot of $\cos(\phi)$ as a function of SNR for the standard algorithm and the beamforming-enhanced algorithm for all choices of Δ_{f} . One plot is shown for both the Class 2 and Class 3 breast phantoms. The quality metric $\cos(\phi)$ is averaged across the four noise instances. For both phantoms, the performance of the standard algorithm is nearly identical to the performance of the beamforming-enhanced algorithm with $\Delta_{\mathrm{f}} = 1$ cm for high SNR, as both quality curves converge asymptotically to a value between 0.8 and 0.83. As SNR decreases, the quality of the standard beamforming reconstruction degrades more than the quality of the beamforming-enhanced reconstruction. This results in a significant quality difference at SNR below 15 dB. The beamforming-enhanced algorithm performs progressively worse for all values of SNR as the focal spacing is increased from 1 cm to 3 cm.

Figs. 7.2 and 7.3 show coronal cross-sections through the exact and reconstructed dielectric profiles for the Class 2 and Class 3 phantoms, respectively. The top row in each figure shows cross sections through the exact profile. The second and third rows show standard DBIM reconstructions at 30 dB and 10 dB SNR, respectively. The fourth and fifth rows show beamforming-enhanced reconstructions with $\Delta_{\mathrm{f}} = 1$ cm for 30 dB an 10 dB SNR, respectively. Each profile is depicted in terms of Debye parameter $\Delta\varepsilon$, which is highly correlated with ε_∞ and σ_s for both the exact and reconstructed profiles. Low-dielectric regions in the profiles correspond to adipose tissue. Both the standard and beamforming-enhanced reconstructions are very visually similar to the exact profiles for 30 dB SNR in that they are accurate in basic shape and location of fibroglandular regions. For the 10 dB SNR case, the standard DBIM reconstructions have degraded considerably. Significant portions of fibroglandular tissue have disappeared in the low-SNR reconstruction for the Class 2 phantom, whereas the fibroglandular regions in the low-SNR reconstructions of the Class 3 phantom have completely changed in shape for several cross-sections. Conversely, the low-SNR beamforming-enhanced reconstructions are very similar to the high-SNR reconstructions for both phantom classes.

Table 7.1: Total number of foci for each choice of Δ_{f}

	$\Delta_{\mathrm{f}} = 1$ cm	$\Delta_{\mathrm{f}} = 2$ cm	$\Delta_{\mathrm{f}} =3$ cm
Class 2	500	57	22
Class 3	306	34	14

The superior fidelity of the beamforming-enhanced algorithm for SNR below 15 dB is significant, as the experimental signal-to-model-error ratio γ as given in Chapter 4 for the miniaturized patch antenna array was comparable to 15 dB for the lower frequency band and significantly less than 15 dB for the upper band. The beamforming-enhanced algorithm thus shows promise for improving the accuracy of experimental microwave dielectric reconstructions. In order to design beamforming weights for the experimental imaging case with the goal of decreasing the sensitivity of the algorithm to model error, it may be necessary to characterize the model-error covariance matrix for the set of signal channels from each transmit antenna.

Table 7.1 gives the total number of foci for each choice of Δ_{f}. Fig. 7.4 shows cross-sections through the beamforming-enhanced DBIM reconstruction for the Class 2 phantom at 30 dB SNR using Δ_{f} =1, 2, and 3 cm. As the focal spacing increases, some fibroglandular features are not resolved, leading to a degradation of the accuracy of the reconstruction. Improving the quality of the beamforming-enhanced reconstructions comes at the cost of a larger computational burden for the inverse solver. However, the number of foci for the densest attempted focal distribution is still significantly smaller than the number of channels used for the standard algorithm. Thus, for a focal spacing of 1 cm, the beamforming-enhanced algorithm offers superior noise performance while requiring a smaller computational cost.

Improvements to the beamforming-enhanced results could hypothetically be achieved by an even denser distribution of foci. However, it is reasonable to assume that there will come a point of diminishing returns to noise insensitivity as focal spacing is decreased. Further improvements may be achieved by using a non-uniform distribution of foci or by implementing row weighting into the algorithm in order to give more or less emphasis in the reconstruction to various regions in the breast.

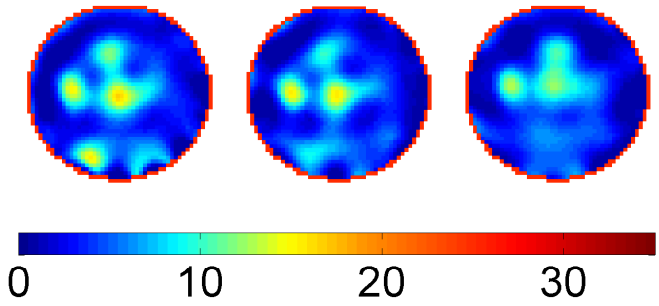

Figure 7.4: Cross-sections through beamforming-enhanced DBIM reconstructions of the Class 2 phantoms. Left: $\Delta_{\mathrm{f}} = 1$ cm. Middle: $\Delta_{\mathrm{f}} = 2$ cm. Right: $\Delta_{\mathrm{f}} = 3$ cm. Debye parameter $\Delta\varepsilon$ is shown. The SNR is 30 dB.

7.5 Conclusion

In this study, a transmit-receive beamforming technique was incorporated into the DBIM algorithm for microwave breast imaging. Beamforming-enhanced DBIM reconstructions of 3-D anatomically-realistic breast phantoms were created and compared to reconstructions using the standard DBIM algorithm. The beamforming-enhanced reconstructions were less sensitive to additive Gaussian white noise. For an SNR of 15 dB or below, the fidelity of the beamforming-enhanced reconstructions were considerably more faithful to the true phantoms. The superior performance of the beamforming-enhanced algorithm in the presence of noise is significant, as the ill-posedness of the inverse system makes it very sensitive to perturbations in the measured signal. Application of the beamforming-enhanced algorithm to experimental data may lead to significant improvements in experimental imaging based on the experimental signal-to-model-error ratios measured in Chapter 4.

Chapter 8

Future Work and Conclusion

8.1 Future work

The results from the previous chapters highlight the promise of mitigating the effect of the ill-posed nature of the microwave breast imaging algorithm using an enclosed array of miniaturized, multi-band patch antennas as well as the beamforming-enhanced inverse scattering algorithm. Challenges remain, however, largely due to degree of model error between measurement and forward solution. In particular, the high degree of model error in the upper frequency band limits the high spatial frequency components that can be incorporated into a dielectric reconstruction, putting an unnecessary limit on the amount of detail that can be seen on an experimental image.

Future work in microwave breast imaging with enclosed arrays of multi-band antennas will address the challenge of model error through research on both hardware and algorithm implementation. Important research directions include the use of alternative slot-loaded patch antenna designs, model error correction through calibration, and experimental implementation of the beamforming-enhanced DBIM.

Exploration of the effects of different slot-loaded patch antenna designs

The results from Chapter 4 show that frequencies in the upper band show a greater degree of mismatch between experimentally acquired signals and simulated signals from the forward solution. It may be that higher frequencies are more prone to model error in general. Errors in array construction, such as bowing of the array panels, may be more significant for shorter wavelengths. Imperfect knowledge of the dielectric properties of the materials in the array, which can change

the overall electrical length of a radiation path in the array cavity, could similarly have more of an effect for shorter wavelengths.

Benefits to the reconstruction may be obtained through using an antenna with resonant bands that are lower in frequency. This may be accomplished by introducing a larger number of slots on the patch antenna surface. In [68, 84, 87], resonant frequencies are shifted downward through the addition of a slot at the center of the antenna, meandering slots on the non-radiating antenna edges, and spirals to the already extant slots along the radiating edges. The lower frequencies are obtained at the expense of progressively more complexity to the patch surface. This added complexity may or may not make modeling the antenna more difficult, thus perhaps partially counteracting the benefits of the lower frequencies. In order to determine to what extent this trade-off exists, it will be necessary to fabricate an array that incorporates one of the more complex antennas and compare experimental versus simulated data in the same fashion as in Chapter 4.

The increase in the number of slots on the patch surface may decrease the gain of the antenna. For a given noise power in the receive channels, this would have the effect of decreasing the SNR. However, the degree of model error already present represents a much larger perturbation in the received signal than would be expected from instrument noise corruption. The trade-off of lower SNR for decreased model error is thus likely a good one. Preliminary reconstructions of breast phantoms from simulated data acquired using different patch antennas suggest that the decrease in gain concomitant with an antenna with more slots doesn't significantly degrade the quality of the resulting image assuming a noise floor that is reasonable for an experimental system [88].

Model error correction through calibration

A degree of model error will be unavoidable due to finite tolerances or subtle user error in construction of the array. It may then be necessary to perform a calibration procedure in order to remove aberrance from the measured signal. Calibration in this manner typically involves acquiring both experimental and simulated data while a known dielectric properties distribution is present in the array. Correction of the measured data from the object to the imaged (i.e., the breast) is then

performed based on the difference between the measured and simulated signals of the known calibration domain. In Chapter 7, calibration between the fine mesh of the data acquisition and the coarse mesh of the forward solution is accomplished by acquiring empty-array data from both meshes. A complex correction factor for each channel is then formed from the ratio of the signals in the different meshes, and the phasors formed by acquiring data from the imaging object are then corrected by multiplying by these complex ratios. This procedure was also used for simulated-data breast imaging studies [57, 59] using an open array of idealized dipoles. A similar procedure has been applied to experimental data in imaging studies using an open array of monopole antennas (e.g., [89]).

Calibrating in this manner is effective assuming a linear scattering environment. Using a cavity-type array, this assumption is less accurate due to the many reflections that occur between the object under test and the conducting ground planes. Thus, an empty array calibration is ineffective for the enclosed array described previously. The array may be effectively calibrated by using a calibration domain other than the empty array. This requires data collection from calibration test objects whose dielectric profiles are known precisely. Array calibrations of this sort have been performed in [90].

For calibration with a test object, it is desired for the fields in the array under the calibration data acquisition to be somewhat similar to the fields in the array when the imaging object is present. This may require the calibration object itself to be somewhat similar to the imaging object. Linear scattering between the two cases is a better approximation in this scenario. For the breast imaging case, a calibration object could be formed following data acquisition from the patient using the thermoplastic mesh, which has conformed to the breast of the human subject. A bag of fluid could then be placed in the thermoplastic mesh for the calibration data acquisition. The fluid could be a solution of water and glycerol or Triton X-100 with a concentration chosen to mimic the assumed average dielectric properties of the breast interior.

Pre-clinical evaluation of the calibration technique could be performed by computing the perturbation metric (4.4) between simulated data and calibrated experimental data acquired from an

imaging object of known dielectric properties, such as the MRI-derived 3-D-printed breast phantom from Chapter 6. The calibration test object in this case would be the conformal thermoplastic mesh filled with a bag of fluid whose dielectric properties represented the mean properties of the 3-D-printed phantom. If γ for the calibrated case is significantly higher than for the uncalibrated case, this would suggest that the calibration procedure is effective. Imaging with the calibrated data (perhaps without using penalties for the upper frequency band) would then be used to evaluate whether the calibration technique leads to higher-quality images.

Experimental implementation of beamforming-enhanced DBIM

The results from Chapter 7 demonstrate that adding the beamforming-enhancement to the DBIM leads to significant imaging improvement when Gaussian white noise is added to the simulated data acquisition measurements at levels corresponding to the levels of model error perturbation from Chapter 4. Applying the beamforming-enhanced DBIM to experimental data may therefore lead to decreased sensitivity to model error. The beamforming weights may be designed using (7.10). The noise covariance matrix $\mathbf{\Sigma}$ may be initially assumed to be the identity matrix. However, the model error in various channels may in fact be correlated. Estimating this correlation, and therefore estimating $\mathbf{\Sigma}$, may then be necessary to optimize performance. This may be accomplished by acquiring experimental and simulated data for several objects of known dielectric properties distribution. The experimental beamforming-enhanced DBIM could then be used to image the simple objects from Chapter 5 or the printed breast phantom from Chapter 6 to determine whether the beamforming enhancement leads to better image quality in the presence of significant model error.

8.2 Conclusion

Microwave breast imaging remains a promising alternative modality for breast density evaluation, breast cancer screening, and treatment monitoring. Overcoming challenges due to the sensitivity of the imaging technique to modest signal corruption requires advancements in hardware

and algorithm design. This document reported a series of studies completed with these goals in mind.

In Chapter 3, a numerical imaging study was performed using an enclosed array of slot-loaded patch antennas. The array elements were designed in order to provide dense spatial sampling of electric fields at multiple frequencies of interest while maintaining efficient transmission. These factors help to decrease the degree of ill-posedness of the linear system of equations which must be solved to find an estimate for the unknown dielectric profile of the target. The conducting ground planes on each array panel shield the imaging environment from outside interference. Successful reconstruction of anatomically realistic numerical breast phantoms demonstrate the theoretical feasibility of microwave breast imaging with such an array.

In Chapter 4, an experimental array prototype was characterized in order to quantify the degree to which model error corrupts the array's scattered signals. The results showed that the degree of model error was more significant than the degree to which instrument noise is expected to corrupt the measured signals. A sensitivity study was also performed, in which various array features were perturbed in simulation in order to determine which features were most likely to lead to significant model error. Immersion medium dielectric properties were shown to have the most corrupting effect.

A series of geometrically simple objects were imaged based on experimental data acquisition with the array prototype in Chapter 5. The resulting dielectric reconstructions were very faithful to the actual dielectric profiles of the targets. The results demonstrated the basic soundness of imaging with the array prototype, and also showed the importance of windowing late-time reflections from the data acquisition to create a quality image.

Chapter 6 described the procedure for constructing a 3-D-printed breast phantom from an MRI-derived numerical breast phantom. The phantom serves as a pre-clinical intermediate imaging case, in which the dielectric distribution of the target is derived from a realistic distribution of tissue. The phantom was then successfully imaged, demonstrating the ability of the array to accurately image targets that achieve a biologically relevant complexity while sacrificing a degree of realism in constituent dielectric properties.

Lastly, a beamforming enhancement to the DBIM was implemented and evaluated in Chapter 7. The goal of the beamforming technique was to synthetically focus the measured signal in order to decrease the effect of signal corruption on the resulting image. Performance was evaluated by imaging numerical breast phantoms from a simulated data acquisition with both the beamforming-enhanced and standard DBIM. The results showed that the beamforming-enhanced algorithm is much less sensitive to noise in an SNR regime that is comparable to the level of signal corruption expected from model error from the prototype array.

Future work on microwave inverse scattering for the breast will involve decreasing the impact of model error. Exploring different slot-loaded patch antenna designs and calibration techniques may yield important benefits in this regard. Experimental implementation of the beamforming-enhanced algorithm may make the algorithm less sensitive to model error, as well. This enhancement may require characterization of the correlation between model error phasors for different transmit-receive channels of the array.

LIST OF REFERENCES

[1] E. Zastrow, S. Davis, M. Lazebnik, F. Kelcz, B. Van Veen, and S. Hagness, "Development of anatomically realistic numerical breast phantoms with accurate dielectric properties for modeling microwave interactions with the human breast," *Biomedical Engineering, IEEE Transactions on*, vol. 55, no. 12, pp. 2792–2800, 2008.

[2] S. Altekruse, C. Kosary, M. Krapcho, N. Neyman, R. Aminou, W. Waldron, J. Ruhl, N. Howlader, Z. Tatalovich, H. Cho, A. Mariotto, M. Eisner, D. Lewis, K. Cronin, H. Chen, E. Feuer, D. Stinchcomb, and B. Edwards, *SEER Cancer Statistics Review, 1975-2007*. National Cancer Institute: Bethesda, MD, 2010.

[3] K. Kerlikowske, D. Grady, S. Rubin, C. Sandrock, and V. Ernster, "Efficacy of screening mammography," *The Journal of the American Medical Association*, vol. 273, no. 2, pp. 149–154, 1995.

[4] L. Humphrey, M. Helfand, B. Chan, and S. Woolf, "Breast cancer screening: a summary of the evidence for the US Preventive Services Task Force," *Annals of Internal Medicine*, vol. 137, no. 5, part 1, pp. 347–360, 2002.

[5] H. Nelson, K. Tyne, A. Naik, C. Bougatsos, B. Chan, and L. Humphrey, "Screening for breast cancer: an update for the US Preventive Services Task Force," *Annals of Internal Medicine*, vol. 151, no. 10, pp. 727–737, 2009.

[6] D. Kopans, *Breast Imaging*. Lippincott-Raven, 1998.

[7] J. Elmore, M. Barton, V. Moceri, S. Polk, P. Arena, and S. Fletcher, "Ten-year risk of false positive screening mammograms and clinical breast examinations," *New England Journal of Medicine*, vol. 338, no. 16, pp. 1089–1096, 1998.

[8] C. Lerman, B. Track, B. Rimer, A. Boyce, C. Jepson, and P. Engstrom, "Psychological and behavioral implications of abnormal mammograms," *Annals of Internal Medicine*, vol. 114, no. 8, pp. 657–661, 1991.

[9] S. Destounis, P. DiNitto, W. Logan-Young, E. Bonaccio, M. Zuley, and K. Willison, "Can computer-aided detection with double reading of screening mammograms help decrease the false-negative rate? Initial experience," *Radiology*, vol. 232, no. 2, pp. 578–584, 2004.

[10] P. Huynh, A. Jarolimek, and S. Daye, "The false-negative mammogram.," *Radiographics*, vol. 18, no. 5, pp. 1137–1154, 1998.

[11] J. Elmore, K. Armstrong, C. Lehman, and S. Fletcher, "Screening for breast cancer," *Journal of the American Medical Association*, vol. 293, no. 10, pp. 1245–1256, 2005.

[12] J. Harvey and V. Bovbjerg, "Quantitative assessment of mammographic breast density: Relationship with breast cancer risk," *Radiology*, vol. 230, no. 1, pp. 29–41, 2004.

[13] N. F. Boyd, H. Guo, L. J. Martin, L. Sun, J. Stone, E. Fishell, R. A. Jong, G. Hislop, A. Chiarelli, S. Minkin, *et al.*, "Mammographic density and the risk and detection of breast cancer," *New England Journal of Medicine*, vol. 356, no. 3, pp. 227–236, 2007.

[14] C. Van Gils, J. Hendriks, R. Holland, N. Karssemeijer, J. Otten, H. Straatman, and A. Verbeek, "Changes in mammographic breast density and concomitant changes in breast cancer risk.," *European Journal of Cancer Prevention: the Official Journal of the European Cancer Prevention Organisation (ECP)*, vol. 8, no. 6, pp. 509–515, 1999.

[15] K. Kerlikowske, L. Ichikawa, D. L. Miglioretti, D. S. Buist, P. M. Vacek, R. Smith-Bindman, B. Yankaskas, P. A. Carney, and R. Ballard-Barbash, "Longitudinal measurement of clinical mammographic breast density to improve estimation of breast cancer risk," *Journal of the National Cancer Institute*, vol. 99, no. 5, pp. 386–395, 2007.

[16] Q. Fang, P. Meaney, and K. Paulsen, "Microwave image reconstruction of tissue property dispersion characteristics utilizing multiple-frequency information," *IEEE Transactions on Microwave Theory and Techniques*, vol. 52, no. 8, pp. 1866–1875, 2004.

[17] Q. Fang, P. Meaney, and K. Paulsen, "Singular value analysis of the Jacobian matrix in microwave image reconstruction," *IEEE Transactions on Antennas and Propagation*, vol. 54, no. 8, pp. 2371–2380, 2006.

[18] S. Aguilar, M. Al-Joumayly, J. Shea, N. Behdad, and S. Hagness, "Design of a microwave breast imaging array composed of dual-band miniaturized antennas," in *Proc. XXXth URSI General Assembly and Scientific Symp.*, pp. 1–4, Istanbul, Turkey, 2011.

[19] B. Van Veen and K. Buckley, "Beamforming: A versatile approach to spatial filtering," *IEEE ASSP Magazine*, vol. 5, no. 2, pp. 4–24, 1988.

[20] M. Tofighi and A. Daryoush, "Near field microwave brain imaging," *Electronics Letters*, vol. 37, no. 13, pp. 807–808, 2001.

[21] C. Gilmore, A. Abubakar, W. Hu, T. Habashy, and P. van den Berg, "Microwave biomedical data inversion using the finite-difference contrast source inversion method," *IEEE Transactions on Antennas and Propagation*, vol. 57, no. 5, pp. 1528–1538, 2009.

[22] S. Semenov, A. Bulyshev, A. Souvorov, A. Nazarov, Y. Sizov, R. Svenson, V. Posukh, A. Pavlovsky, P. Repin, and G. Tatsis, "Three-dimensional microwave tomography: experimental imaging of phantoms and biological objects," *IEEE Transactions on Microwave Theory and Techniques*, vol. 48, no. 6, pp. 1071–1074, 2000.

[23] S. Semenov, R. Svenson, V. Posukh, A. Nazarov, Y. Sizov, A. Bulyshev, A. Souvorov, W. Chen, J. Kasell, and G. Tatsis, "Dielectrical spectroscopy of canine myocardium during acute ischemia and hypoxia at frequency spectrum from 100 kHz to 6 GHz," *IEEE Transactions on Medical Imaging*, vol. 21, no. 6, pp. 703–707, 2002.

[24] P. M. Meaney, T. Zhou, D. Goodwin, A. Golnabi, E. A. Attardo, and K. D. Paulsen, "Bone dielectric property variation as a function of mineralization at microwave frequencies," *International Journal of Biomedical Imaging*, vol. 2012, pp. 649612–1649612–9, 2012.

[25] A. Souvorov, A. Bulyshev, S. Semenov, R. Svenson, A. Nazarov, Y. Sizov, and G. Tatsis, "Microwave tomography: A two-dimensional Newton iterative scheme," *IEEE Transactions on Microwave Theory and Techniques*, vol. 46, no. 11, pp. 1654–1659, 1998.

[26] S. Chaudhary, R. Mishra, A. Swarup, and J. Thomas, "Dielectric properties of normal & malignant human breast tissues at radiowave & microwave frequencies.," *Indian Journal of Biochemistry & Biophysics*, vol. 21, no. 1, pp. 76–79, 1984.

[27] A. Campbell and D. Land, "Dielectric properties of female human breast tissue measured in vitro at 3.2 GHz," *Physics in Medicine and Biology*, vol. 37, pp. 193–210, 1992.

[28] J. Choi, J. Cho, Y. Lee, J. Yim, B. Kang, K. Keun Oh, W. Hee Jung, H. Jung Kim, C. Cheon, H. Lee, and Y. Kwon, "Microwave detection of metastasized breast cancer cells in the lymph node; potential application for sentinel lymphadenectomy," *Breast Cancer Research and Treatment*, vol. 86, no. 2, pp. 107–115, 2004.

[29] T. England, "Dielectric properties of the human body for wave-lengths in the 1–10 cm. range," *Nature*, vol. 166, pp. 480–481, 1950.

[30] W. Joines, Y. Zhang, C. Li, and R. Jirtle, "The measured electrical properties of normal and malignant human tissues from 50 to 900 MHz," *Medical Physics*, vol. 21, pp. 547–551, 1994.

[31] A. Surowiec, S. Stuchly, J. Barr, and A. Swarup, "Dielectric properties of breast carcinoma and the surrounding tissues," *IEEE Transactions on Biomedical Engineering*, vol. 35, no. 4, pp. 257–263, 1988.

[32] M. Lazebnik, D. Popovic, L. McCartney, C. Watkins, M. Lindstrom, J. Harter, S. Sewall, T. Ogilvie, A. Magliocco, T. Breslin, W. Temple., D. Mew, J. Booske, M. Okoniewski, and S. Hagness, "A large-scale study of the ultrawideband microwave dielectric properties of normal, benign and malignant breast tissues obtained from cancer surgeries," *Physics in Medicine and Biology*, vol. 52, pp. 6093–6115, 2007.

[33] E. Fear, S. Hagness, P. Meaney, M. Okoniewski, and M. Stuchly, "Enhancing breast tumor detection with near-field imaging," *IEEE Microwave Magazine*, vol. 3, no. 1, pp. 48–56, 2002.

[34] E. Fear, J. Sill, and M. Stuchly, "Experimental feasibility study of confocal microwave imaging for breast tumor detection," *IEEE Transactions on Microwave Theory and Techniques*, vol. 51, no. 3, pp. 887–892, 2003.

[35] E. Fear and M. Stuchly, "Microwave system for breast tumor detection," *IEEE Microwave and Guided Wave Letters*, vol. 9, no. 11, pp. 470–472, 1999.

[36] S. Hagness, A. Taflove, and J. Bridges, "Two-dimensional FDTD analysis of a pulsed microwave confocal system for breast cancer detection: Fixed-focus and antenna-array sensors," *IEEE Transactions on Biomedical Engineering*, vol. 45, no. 12, pp. 1470–1479, 1998.

[37] S. Hagness, A. Taflove, and J. Bridges, "Three-dimensional FDTD analysis of a pulsed microwave confocal system for breast cancer detection: Design of an antenna-array element," *IEEE Transactions on Antennas and Propagation*, vol. 47, no. 5, pp. 783–791, 1999.

[38] M. Hernández-López, M. Quintillán-González, S. González García, A. Rubio Bretones, and R. Gómez Martín, "A rotating array of antennas for confocal microwave breast imaging," *Microwave and Optical Technology Letters*, vol. 39, no. 4, pp. 307–311, 2003.

[39] X. Li and S. Hagness, "A confocal microwave imaging algorithm for breast cancer detection," *IEEE Microwave and Wireless Components Letters*, vol. 11, no. 3, pp. 130–132, 2001.

[40] H. Lim, N. Nhung, E. Li, and N. Thang, "Confocal microwave imaging for breast cancer detection: Delay-multiply-and-sum image reconstruction algorithm," *IEEE Transactions on Biomedical Engineering*, vol. 55, no. 6, pp. 1697–1704, 2008.

[41] R. Nilavalan, A. Gbedemah, I. Craddock, X. Li, and S. Hagness, "Numerical investigation of breast tumour detection using multi-static radar," *Electronics Letters*, vol. 39, pp. 1787–1789, 2003.

[42] P. Kosmas and C. Rappaport, "FDTD-based time reversal for microwave breast cancer detection-localization in three dimensions," *IEEE Transactions on Microwave Theory and Techniques*, vol. 54, no. 4, pp. 1921–1927, 2006.

[43] E. Bond, X. Li, S. Hagness, and B. Van Veen, "Microwave imaging via space-time beamforming for early detection of breast cancer," *IEEE Transactions on Antennas and Propagation*, vol. 51, no. 8, pp. 1690–1705, 2003.

[44] S. Davis, E. Bond, S. Hagness, and B. Van Veen, "Microwave imaging via space-time beamforming for early detection of breast cancer: Beamformer design in the frequency domain," *Journal of Electromagnetic Waves and Applications*, vol. 17, no. 2, pp. 357–381, 2003.

[45] S. Davis, H. Tandradinata, S. Hagness, and B. Van Veen, "Ultrawideband microwave breast cancer detection: a detection-theoretic approach using the generalized likelihood ratio test," *IEEE Transactions on Biomedical Engineering*, vol. 52, no. 7, pp. 1237–1250, 2005.

[46] X. Li, S. Davis, S. Hagness, D. Van Der Weide, and B. Van Veen, "Microwave imaging via space-time beamforming: Experimental investigation of tumor detection in multilayer breast phantoms," *IEEE Transactions on Microwave Theory and Techniques*, vol. 52, no. 8, pp. 1856–1865, 2004.

[47] X. Li, E. Bond, B. Van Veen, and S. Hagness, "An overview of ultra-wideband microwave imaging via space-time beamforming for early-stage breast-cancer detection," *IEEE Antennas and Propagation Magazine*, vol. 47, no. 1, pp. 19–34, 2005.

[48] Y. Xie, B. Guo, L. Xu, J. Li, and P. Stoica, "Multistatic adaptive microwave imaging for early breast cancer detection," *IEEE Transactions on Biomedical Engineering*, vol. 53, no. 8, pp. 1647–1657, 2006.

[49] M. Klemm, J. Leendertz, D. Gibbins, I. Craddock, A. Preece, and R. Benjamin, "Microwave radar-based breast cancer detection: Imaging in inhomogeneous breast phantoms," *Antennas and Wireless Propagation Letters, IEEE*, vol. 8, pp. 1349–1352, 2009.

[50] P. Meaney, M. Fanning, D. Li, S. Poplack, and K. Paulsen, "A clinical prototype for active microwave imaging of the breast," *IEEE Transactions on Microwave Theory and Techniques*, vol. 48, no. 11, pp. 1841–1853, 2000.

[51] P. Meaney, M. Fanning, T. Raynolds, C. Fox, Q. Fang, C. Kogel, S. Poplack, and K. Paulsen, "Initial clinical experience with microwave breast imaging in women with normal mammography," *Academic Radiology*, vol. 14, no. 2, pp. 207–218, 2007.

[52] T. M. Grzegorczyk, P. M. Meaney, P. A. Kaufman, R. di Florio-Alexander, and K. Paulsen, "Fast 3-D tomographic microwave imaging for breast cancer detection," *IEEE Transactions on Medical Imaging*, vol. 31, no. 8, pp. 1584–1592, 2012.

[53] A. Bulyshev, S. Semenov, A. Souvorov, R. Svenson, A. Nazarov, Y. Sizov, and G. Tatsis, "Computational modeling of three-dimensional microwave tomography of breast cancer," *IEEE Transactions on Biomedical Engineering*, vol. 48, no. 9, pp. 1053–1056, 2001.

[54] Q. Fang, P. Meaney, S. Geimer, A. Streltsov, and K. Paulsen, "Microwave image reconstruction from 3-D fields coupled to 2-D parameter estimation," *IEEE Transactions on Medical Imaging*, vol. 23, no. 4, pp. 475–484, 2004.

[55] Z. Zhang and Q. Liu, "Three-dimensional nonlinear image reconstruction for microwave biomedical imaging," *Biomedical Engineering, IEEE Transactions on*, vol. 51, no. 3, pp. 544–548, 2004.

[56] T. Rubæk, O. Kim, and P. Meincke, "Computational validation of a 3-D microwave imaging system for breast-cancer screening," *IEEE Transactions on Antennas and Propagation*, vol. 57, no. 7, pp. 2105–2115, 2009.

[57] J. Shea, P. Kosmas, S. Hagness, and B. Van Veen, "Three-dimensional microwave imaging of realistic numerical breast phantoms via a multiple-frequency inverse scattering technique," *Medical Physics*, vol. 37, pp. 4210–4226, 2010.

[58] W. Chew and Y. Wang, "Reconstruction of two-dimensional permittivity distribution using the distorted Born iterative method," *IEEE Transactions on Medical Imaging*, vol. 9, no. 2, pp. 218–225, 1990.

[59] J. Shea, P. Kosmas, B. Van Veen, and S. Hagness, "Contrast-enhanced microwave imaging of breast tumors: A computational study using 3D realistic numerical phantoms," *Inverse Problems*, vol. 26, p. 074009, 2010.

[60] A. Mashal, J. H. Booske, and S. C. Hagness, "Toward contrast-enhanced microwave-induced thermoacoustic imaging of breast cancer: An experimental study of the effects of microbubbles on simple thermoacoustic targets," *Physics in medicine and biology*, vol. 54, no. 3, pp. 641–650, 2009.

[61] A. Mashal, B. Sitharaman, X. Li, P. K. Avti, A. V. Sahakian, J. H. Booske, and S. C. Hagness, "Toward carbon-nanotube-based theranostic agents for microwave detection and treatment of breast cancer: Enhanced dielectric and heating response of tissue-mimicking materials," *IEEE Transactions on Biomedical Engineering*, vol. 57, no. 8, pp. 1831–1834, 2010.

[62] J. Johnson, T. Takenaka, and T. Tanaka, "Two-dimensional time-domain inverse scattering for quantitative analysis of breast composition," *IEEE Transactions on Biomedical Engineering*, vol. 55, no. 8, pp. 1941–1945, 2008.

[63] J. Johnson, T. Takenaka, K. Ping, S. Honda, and T. Tanaka, "Advances in the 3-D forward–backward time-stepping (FBTS) inverse scattering technique for breast cancer detection," *IEEE Transactions on Biomedical Engineering*, vol. 56, no. 9, pp. 2232–2243, 2009.

[64] R. Remis and P. van den Berg, "On the equivalence of the Newton-Kantorovich and distorted Born methods," *Inverse Problems*, vol. 16, no. 1, pp. L1–L4, 2000.

[65] M. Burfeindt, N. Behdad, B. Van Veen, and S. C. Hagness, "Quantitative microwave imaging of realistic numerical breast phantoms using an enclosed array of multi-band, miniaturized patch antennas," *IEEE Antennas and Wireless Propagation Letters*, vol. 11, pp. 1626–1629, 2012.

[66] P. Mojabi and J. LoVetri, "A novel microwave tomography system using a rotatable conductive enclosure," *IEEE Transactions on Antennas and Propagation*, vol. 59, no. 5, pp. 1597–1605, 2011.

[67] M. Haynes, J. Stang, and M. Moghaddam, "Microwave breast imaging system prototype with integrated numerical characterization," *International Journal of Biomedical Imaging*, vol. 2012, pp. 1–18, 2012.

[68] M. Al-Joumayly, S. Aguilar, N. Behdad, and S. Hagness, "Dual-band miniaturized patch antennas for microwave breast imaging," *IEEE Antennas and Wireless Propagation Letters*, vol. 9, pp. 268–271, 2010.

[69] S. Aguilar, J. Shea, M. Al-Joumayly, B. Van Veen, N. Behdad, and S. Hagness, "Dielectric characterization of PCL-based thermoplastic materials for microwave diagnostic and therapeutic applications," *IEEE Transactions on Biomedical Engineering*, vol. 59, no. 3, pp. 627–633, 2012.

[70] S. Maci, G. Biffi Gentili, P. Piazzesi, and C. Salvador, "Dual-band slot-loaded patch antenna," *IEE Proceedings on Microwaves, Antennas, and Propagation*, vol. 142, no. 3, pp. 225–232, 1995.

[71] J. Stang and W. Joines, "Tapered microstrip patch antenna array for microwave breast imaging," in *Proc. IEEE MTT-S Int. Microw. Symp. Dig*, pp. 1313–1316, 2008.

[72] D. Winters, J. Shea, E. Madsen, G. Frank, B. Van Veen, and S. Hagness, "Estimating the breast surface using UWB microwave monostatic backscatter measurements," *IEEE Transactions on Biomedical Engineering*, vol. 55, no. 1, pp. 247–256, 2008.

[73] S. Gabriel, R. Lau, and C. Gabriel, "The dielectric properties of biological tissues: III. Parametric models for the dielectric spectrum of tissues," *Physics in Medicine and Biology*, vol. 41, pp. 2271–2293, 1996.

[74] S.-Y. Huang, J. M. Boone, K. Yang, N. J. Packard, S. E. McKenney, N. D. Prionas, K. K. Lindfors, and M. J. Yaffe, "The characterization of breast anatomical metrics using dedicated breast ct," *Medical Physics*, vol. 38, no. 4, pp. 2180–2191, 2011.

[75] D. Pozar, *Microwave Engineering*, ch. 4, p. 192. Wiley, 2012.

[76] K. Kurokawa, "Power waves and the scattering matrix," *IEEE Transactions on Microwave Theory and Techniques*, vol. 13, no. 2, pp. 194–202, 1965.

[77] M. Burfeindt, T. Colgan, R. Mays, J. Shea, N. Behdad, B. Van Veen, and S. Hagness, "MRI-derived 3-D-printed breast phantom for microwave breast imaging validation," *IEEE Antennas and Wireless Propagation Letters*, vol. 11, pp. 1610–1613, 2012.

[78] M. Haynes, S. Clarkson, and M. Moghaddam, "Electromagnetic inverse scattering algorithm and experiment using absolute source characterization," *IEEE Transactions on Antennas and Propagation*, vol. 60, no. 4, pp. 1854–1867, 2012.

[79] M. Miyakawa, S. Takata, and K. Inotsume, "Development of non-uniform breast phantom and its microwave imaging for tumor detection by CP-MCT," in *Proc. Annual International Conference IEEE EMBS*, pp. 2723–2726, Minneapolis, MN, 2009.

[80] A. Golnabi, P. Meaney, N. Epstein, and K. Paulsen, "Microwave imaging for breast cancer detection: Advances in three-dimensional image reconstruction," in *Proc. Annual International Conference of the IEEE EMBS*, pp. 5730–5733, Prague, Czech Republic, 2011.

[81] J. Croteau, J. Sill, T. Williams, and E. Fear, "Phantoms for testing radar-based microwave breast imaging," in *Proc. 13th International Symposium on Antenna Technology and Applied Electromagentics and the Canadian Radio Science Meeting*, pp. 1–4, Toronto, Canada, 2009.

[82] A. Mashal, F. Gao, and S. Hagness, "Heterogeneous anthropomorphic phantoms with realistic dielectric properties for microwave breast imaging experiments," *Microwave and Optical Technology Letters*, vol. 53, no. 8, pp. 1896–1902, 2011.

[83] M. Lazebnik, E. Madsen, G. Frank, and S. Hagness, "Tissue-mimicking phantom materials for narrowband and ultrawideband microwave applications," *Physics in Medicine and Biology*, vol. 50, no. 18, pp. 4245–4258, 2005.

[84] M. A. Al-Joumayly, S. M. Aguilar, N. Behdad, and S. C. Hagness, "Multi-band, miniaturized patch antenna elements for microwave breast imaging applications," in *IEEE International Symposium on Antennas and Propagation and USNC/URSI National Radio Science Meeting, Spokane, WA*, 2011.

[85] A. Abubakar, T. M. Habashy, and G. Pan, "Microwave data inversions using the source-receiver compression scheme," *Antennas and Propagation, IEEE Transactions on*, vol. 60, no. 6, pp. 2853–2864, 2012.

[86] T. Rubæk, P. Meaney, P. Meincke, and K. Paulsen, "Nonlinear microwave imaging for breast-cancer screening using Gauss–Newton's method and the CGLS inversion algorithm," *IEEE Transactions on Antennas and Propagation*, vol. 55, no. 8, pp. 2320–2331, 2007.

[87] M. A. Al-Joumayly, S. M. Aguilar, N. Behdad, and S. C. Hagness, "Miniaturized patch antennas with multi-bands of operation for microwave breast imaging," in *34th Annual Antenna Applications Symposium, Monticello, IL*, 2010.

[88] S. Aguilar, M. Burfeindt, N. Behdad, and S. Hagness, "Multi-band miniaturized patch antennas for a compact, shielded microwave breast imaging array," *IEEE Transactions on Antennas and Propagation*, in revision, 2013.

[89] P. M. Meaney, K. D. Paulsen, and J. T. Chang, "Near-field microwave imaging of biologically-based materials using a monopole transceiver system," *IEEE Transactions on Microwave Theory and Techniques*, vol. 46, no. 1, pp. 31–45, 1998.

[90] M. Ostadrahimi, P. Mojabi, C. Gilmore, A. Zakaria, S. Noghanian, S. Pistorius, and J. LoVetri, "Analysis of incident field modeling and incident/scattered field calibration techniques in microwave tomography," *IEEE Antennas and Wireless Propagation Letters*, vol. 10, pp. 900–903, 2011.